

# FLAIM: a reduced volume ignition model for the compression and thermonuclear burn of spherical fuel capsules

Abd Essamade Saufi<sup>a,\*</sup>, Hannah Bellenbaum<sup>a,1</sup>, Martin Read<sup>a</sup>, Nicolas Niasse<sup>a</sup>, Sean Barrett<sup>a</sup>, Nicholas Hawker<sup>a</sup>, Nathan Joiner<sup>a</sup>, David Chapman<sup>a</sup>

<sup>a</sup>*First Light Fusion Ltd., Unit 9/10, Oxford Pioneer Park, Mead Road, Oxford, OX5 1QU, Oxfordshire, United Kingdom (UK)*

---

## Abstract

We present the “First Light Advanced Ignition Model” (FLAIM), a reduced model for the implosion, adiabatic compression, volume ignition and thermonuclear burn of a spherical DT fuel capsule utilising a high-Z metal pusher. FLAIM is characterised by a highly modular structure, which makes it an appropriate tool for optimisations, sensitivity analyses and parameter scans. One of the key features of the code is the 1D description of the hydrodynamic operator, which has a minor impact on the computational efficiency, but allows us to gain a major advantage in terms of physical accuracy. We demonstrate that a more accurate treatment of the hydrodynamics plays a primary role in closing most of the gap between a simple model and a general 1D rad-hydro code, and that only a residual part of the discrepancy is attributable to the heat losses. We present a detailed quantitative comparison between FLAIM and 1D rad-hydro simulations, showing good agreement over a large parameter space in terms of temporal profiles of key physical quantities, ignition maps and typical burn metrics.

*Keywords:* ICF, volume ignition, robustness, high-Z pusher, simple model,

---

\*Corresponding author

*Email address:* [abdessamade.saufi@firstlightfusion.com](mailto:abdessamade.saufi@firstlightfusion.com) (Abd Essamade Saufi)

<sup>1</sup>Present address: Center for Advanced Systems Understanding (CASUS), D-02826 Görlitz, Germany; Helmholtz-Zentrum Dresden-Rossendorf (HZDR), D-01328 Dresden, Germany

Revolver

---

## 1. Introduction

First Light Fusion (FLF) is a privately-funded research company working on alternative solutions for inertial confinement fusion (ICF) [1]. Part of FLF’s current effort is devoted to the development of numerical capabilities to quickly iterate and perform sensitivity analyses on the design of our drivers and targets, which requires the systematic exploration of a vast multi-dimensional parameter space at low cost. A fundamental step is the development of *simplified* models, that can run rapidly, and whose aim is to capture in broad terms the physical phenomena involved in a general end-to-end system (e.g., from the driver physics to fuel ignition and burn). The objective is to adopt these models as *auxiliary* tools, to help inform the approximate shape of the hyper-surface of a general performance metric (e.g., neutron yield), immediately identify non-viable configurations and eventually refine the analysis with standard rad-hydro simulations focusing on the most relevant regions.

The platform is based on *volume ignition*, in particular on the Revolver concept [2, 3, 4]: using a high-Z metal pusher to confine the fuel, instead of the cold DT shell typical of hot-spot ignition designs, one sacrifices high-gain for robustness, i.e., lower losses, lower ignition temperature and lower implosion velocity [5]. Whilst simple reduced models for hot-spot ignition are numerous, analogous models for volume ignition are less common [6, 7, 8, 9], and frequently lack robust comparison against high-fidelity simulations in order to assess their accuracy.

In this context, the objective of this work is two-fold. Firstly, we present the “First Light Advanced Ignition Model” (FLAIM), a reduced model describing the implosion, volume ignition and thermonuclear burn of a spherical fuel capsule compressed by a high-Z pusher. It includes the use of non-ideal tabulated equations of state (EoS) and transport properties, 1D treatment of the hydrodynamics, a novel approach for the wall modelling, which removes the assumption of thermodynamic equilibrium between the wall and the radiation field, and a thermonuclear burn operator. From an implementation perspective, FLAIM’s main strengths are (i) flexibility, (ii) modularity of the code structure and (iii) computational efficiency, which makes it suitable for large parameter scans and sensitivity analyses. Secondly, we present a thorough analysis on the accuracy of FLAIM with respect to high-fidelity 1D simulations in a large design space. In particular, we highlight the primary role that the hydrodynamic has on the physics of the system, as well as

the negative impact that approximate treatments of the hydrodynamics may have on the predictive capability of the model when used to explore ignition regions.

The paper's organisation reflects this purpose, including: a detailed description of the mathematical model and the physical operators (Section 2) and a brief presentation on the numerical methodology, code structure and implementation (Section 3). Section 4 presents a detailed investigation on the accuracy of **FLAIM**'s hydrodynamic operator by means of cross-code comparison with our in-house hydrodynamic code **B2**. The analysis is completed in Sections 5-6 by considering the accuracy of simulations of igniting targets, and demonstrating the reliability of **FLAIM** as a reduced ignition model, comparing the main key diagnostic quantities for the Revolver design with reference results reported in literature.

## 2. Mathematical model

In this section, the mathematical model implemented in **FLAIM** is derived and presented. Figure 1 represents the main physical and geometric quantities defining the system: the fuel is a DT mixture (with number densities  $n_D, n_T$ ) described using a 3-temperature approach (ion  $T_i$ , electron  $T_e$ , radiation  $T_r$ ). Based on results from 1D simulations, the high-Z pusher material can be sensibly assumed to have a single temperature  $T_p$ . These physical quantities are to be interpreted as *volume-averaged* over the domain of interest, defining a 0D model. The relevant conserved quantities are evolved over time by physical operators comprising (i) hydrodynamics, (ii) thermal equilibration, (iii) wall, (iv) thermal conduction, (v) radiation loss and (vi) thermonuclear burn. All of the operators have been independently verified against simple benchmark test cases and tested for global mass and energy conservation.

### 2.1. Hydrodynamics

Focusing on the fuel region first (Figure 1), we consider a spherical volume  $V_f$  enclosed by a surface  $S_1$  on which a pressure  $p_f = p_i + p_e + p_r$  is exerted. The following equations describe the temporal variation of total mass,  $N_S$  species number, momentum and internal energy in the system:

$$\frac{d}{dt} \int_{V_f} \rho_f dV_f = 0, \quad (1)$$

$$\frac{d}{dt} \int_{V_f} n_j dV_f = 0 \quad \text{for } j = 0, \dots, N_S, \quad (2)$$

$$\frac{d}{dt} \int_{V_f} \rho_f \mathbf{v} dV_f = - \int_{S_1} p_f \hat{\mathbf{n}} dS_1, \quad (3)$$

$$\frac{d}{dt} \int_{V_f} u_f dV_f = - \int_{V_f} p_f (\nabla \cdot \mathbf{v}) dV_f. \quad (4)$$

Introducing the volume-averaged quantities for the mass density  $\rho$ , species number densities  $n_j$ , momentum density  $\rho \mathbf{v}$  and internal energy density  $u$ , and assuming a uniform pressure distribution<sup>2</sup>,

---

<sup>2</sup>We are omitting the macron for the average to avoid overcomplicating the mathematical notation.

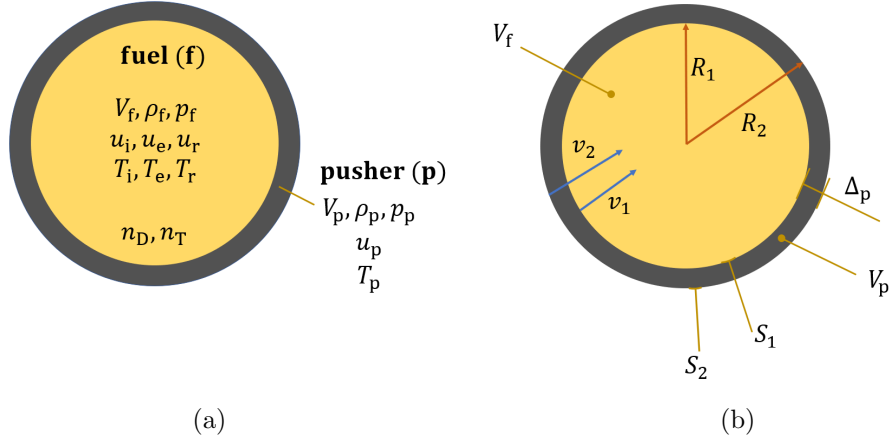


Figure 1: Main physical and geometrical quantities defining the closed system fuel + pusher.

$$\frac{d(\rho_f V_f)}{dt} = 0, \quad (5)$$

$$\frac{d(n_j V_f)}{dt} = 0 \quad \text{for } j = 0, \dots, N_S, \quad (6)$$

$$\frac{d(\rho_f \mathbf{v} V_f)}{dt} = -p_f \int_{S_1} \hat{\mathbf{n}} dS_1 = \mathbf{0}, \quad (7)$$

$$\frac{d(u_f V_f)}{dt} = -p_f \int_{S_1} \mathbf{v} \cdot \hat{\mathbf{n}} dS_1 = -p_f v_1 S_1, \quad (8)$$

where the global momentum equation becomes trivial under spherical symmetry. Noticing that, for a sphere,  $dV/dt = vS$ , one finally obtains the equations for the volume-averaged mass density, species number densities and internal energy density of the fuel:

$$\frac{d\rho_f}{dt} = -\rho_f v_1 \frac{S_1}{V_f}, \quad (9)$$

$$\frac{dn_j}{dt} = -n_j v_1 \frac{S_1}{V_f} \quad \text{for } j = 0, \dots, N_S, \quad (10)$$

$$\frac{du_f}{dt} = -(p_f + u_f) v_1 \frac{S_1}{V_f}, \quad (11)$$

where the additional term  $u_f v_1 (S_1/V_f)$  arises because we are solving for a quantity per unit volume [10]. The energy equation is separately solved for each fluid component (ion, electron, radiation)<sup>3</sup>,

$$\frac{du_k}{dt} = -(p_k + u_k) v_1 \frac{S_1}{V_f} \quad \text{for } k \in \{i, e, r\}, \quad (12)$$

whose sum provides Equation 11. The same exercise can be applied (without  $n_j$ ) to the spherical shell volume  $V_p$  representing the pusher region (Figure 1), leading to the following equations:

$$\frac{d\rho_p}{dt} = -\rho_p \frac{v_2 S_2 - v_1 S_1}{V_p}, \quad (13)$$

$$\frac{du_p}{dt} = -(p_p + u_p) \frac{v_2 S_2 - v_1 S_1}{V_p}. \quad (14)$$

This set of equations must be augmented with kinematic equations for the radii  $R_1, R_2$ ,

$$\frac{dR_k}{dt} = v_k \quad \text{for } k \in \{1, 2\}, \quad (15)$$

and two equations of state to link the mass and internal energy densities to the thermodynamic pressure for the two materials,

$$\mathcal{F}_k(\rho_k, u_k, p_k) = 0 \quad \text{for } k \in \{f, p\}. \quad (16)$$

Our 2T EoS is based on the Frankfurt EoS (FEOS) package [11], which derives from the Quotidian EoS (QEoS) framework [12] and is tabulated for temperatures up to  $T_i = 100$  keV. Finally, one has to include equations for the surface velocities  $v_1, v_2$  to close the system. Depending on how the equation for the implosion velocity is derived, three different hydrodynamic models can be defined, which determine the dynamics of  $v_1, v_2$ .

---

<sup>3</sup>The subscript “f” for the fuel individual components is dropped to simplify the mathematical notation. Since the pusher has a single temperature  $T_p$ , this is unambiguous.

### 2.1.1. Hydrodynamic model 0

This is one of the most widely used hydrodynamics treatments for reduced ignition models [8, 9], in which an incompressible pusher with finite mass and an infinitesimally small thickness is assumed ( $\Delta_p \rightarrow 0$ ). The fuel kinetic energy is considered to be zero. Therefore, the only force decelerating the pusher derives from the fuel pressure exerted on the surface  $S_1$ ,

$$m_p \frac{dv_1}{dt} = p_f S_1. \quad (17)$$

This model provides no information on the state of the pusher during the implosion phase, assuming its internal energy is constant. This poses serious problems in terms of energy distribution in the system, since geometry convergence is essentially neglected.

We report this model for the sake of completeness, since its inadequacy has been considered in previous works [13, 14] in the context of hot-spot ignition, and it will not be investigated any further.

### 2.1.2. Hydrodynamic model I

In this model we remove the assumption of an incompressible pusher with zero thickness, introducing a compressible pusher with a finite volume and a spatially uniform velocity profile, which thus has a *constant thickness*. The initial work of Kirkpatrick and Wheeler adopted this approach [15, 6], limiting however the analysis to thin shells. In this case  $v_1 = v_2$ , and an equation for the interface velocity  $v_1$  can be obtained imposing the conservation of the total energy  $E_{\text{tot}}$  (assuming a closed thermodynamic system),

$$\frac{dE_{\text{tot}}}{dt} = \frac{d(K_p + U_p + K_f + U_f)}{dt} = 0, \quad (18)$$

where the total kinetic and internal energies are respectively defined as  $K_i = k_i V_i$  and  $U_i = u_i V_i$  for  $i \in \{f, p\}$ . The assumption of flat velocity profile provides  $dK_p/dt = m_p v_1 (dv_1/dt)$ , whilst from Equations 11, 14 we can write  $dU_p/dt = -p_p v_1 (S_2 - S_1)$  and  $dU_f/dt = -p_f v_1 S_1$ . Following Kirkpatrick's approach of assuming a linear velocity profile in the fuel region<sup>4</sup>, we can write  $dK_f/dt = (3/5) m_f v_1 (dv_1/dt)$ . Therefore, we obtain

---

<sup>4</sup>This is also substantiated analysing 1D hydrodynamic simulations carried out with our in-house hydrodynamic code B2 (Section 4). Specifically, assuming a profile  $v(r) = v_1 \frac{r}{R_1}$ , the fuel kinetic energy can be written as  $K_f = \frac{1}{2} \rho_f \int_0^{R_1} 4\pi r^2 v^2(r) dr$ .



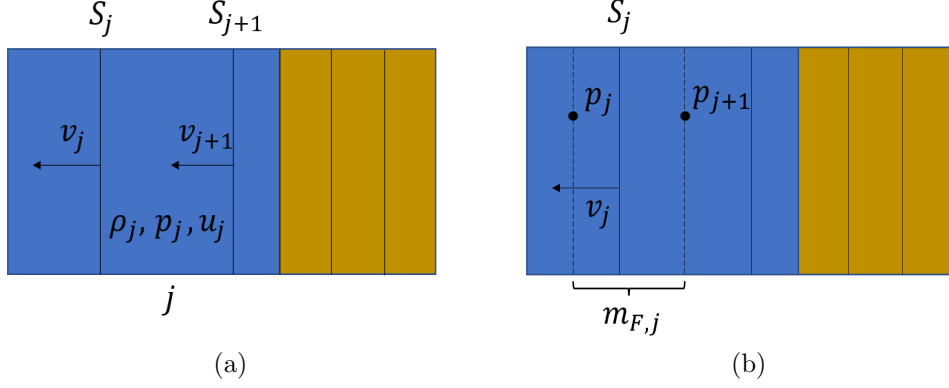


Figure 2: Discretisation of fuel and pusher region using a staggered grid (a). Physical quantities necessary to define the momentum equation (Equation 22) (b).

$$\left( m_p + \frac{3}{5} m_f \right) \frac{dv_1}{dt} = p_f S_1 + p_p (S_2 - S_1) , \quad (19)$$

which reverts back to Equation 17 if  $S_2 = S_1$  (and neglecting  $K_f$ ), i.e., when the pusher has a vanishing volume.

### 2.1.3. Hydrodynamic model II

Moving away from the constant-thickness pusher assumption can be challenging, since the only physical arguments available to link the two velocities  $v_1, v_2$  is momentum conservation, which we initially discarded. The strategy followed in work is to derive a non-uniform velocity profile in the pusher is to discretise the whole target in  $N_c = N_{c,f} + N_{c,p}$  (fuel + pusher) concentric fluid elements (cells) whose masses are constant (in time) and comoving with the fluid. This is a Lagrangian representation of the hydrodynamics, which allows one to efficiently model situations in which the material strongly compresses or expands. This representation is particularly advantageous in 1D and, mathematically, allows one to ignore the advection term in the transport equations. For each fluid element  $j$ :

$$\frac{d\rho_j}{dt} = -\frac{\rho_j}{V_j} (v_{j+1}S_{j+1} - v_jS_j) , \quad (20)$$

$$\frac{du_{k,j}}{dt} = -(p_{k,j} + u_{k,j}) \frac{v_{j+1}S_{j+1} - v_jS_j}{V_j} \quad \text{for } k \in \{\text{i, e, r}\} . \quad (21)$$

Name	Description	Equations
Hydro 0	Volume averaged 0D model. Pusher thickness is zero. $v_p(t, r) = 0$ .	9, 10, 12, 15, 17
Hydro I	Volume averaged 0D model. Pusher thickness is constant. $v_p(t, r) = v_1(t) = v_2(t)$ . $v_p(t, r)$ derived from global energy conservation.	9, 10, 12, 13, 14, 15, 19
Hydro II	1D Lagrangian model with artificial viscosity. Pusher thickness is variable. $v_p(t, r) = \mathcal{F}(t, r)$ . $v_p(t, r)$ derived from momentum conservation.	10, 20, 21, 22, 23

Table 1: Summary of the hydrodynamic models investigated in this work and corresponding equations.

We adopt a staggered grid approach (Figure 2), in which all quantities are stored at the cell centres, except for velocities, which are stored at face centres. The grid motion is provided by Equation 15 (for each face, i.e.,  $k = j$ ), whilst the fluid elements interact via momentum transfer,

$$\frac{dv_j}{dt} = \frac{p_j - p_{j+1}}{m_{F,j}} S_j, \quad (22)$$

in which a projected face-centred mass  $m_{F,j}$  represents the inertia of face  $j$  subjected to the local pressure difference  $p_j - p_{j+1}$  (Figure 2b). The boundary conditions are simply  $v_0 = 0$  (fuel centre) and  $p_{N_c+1} = 0$  (enforced by a ghost cell  $j = N_c + 1$  at the outer boundary). Some form of artificial viscosity is necessary to capture shocks and avoid unphysical oscillations in the vicinity of hydrodynamic discontinuities. The basic form from Von Neumann et al. [16] is adopted, in which a pseudo-pressure  $p^*$ , defined as

$$p^* = \rho c_q \Delta x^2 \left( \frac{dv}{dx} \right)^2 \quad \text{if } \frac{dv}{dx} < 0, \quad (23)$$

is added to the thermodynamic pressure  $p$  (in Equations 21, 22) if the flow is compressive. Artificial viscosity is responsible for the entropy production, and its dissipative nature is a direct result of the requirement for the shock

to have a finite width in terms of grid spacing  $\Delta x$  (the constant is chosen to be  $c_q = 2$ , corresponding to  $\sim 3 - 4$  cell thick shocks [17]).

Since the remaining operators in **FLAIM** evolve integrated conserved quantities, it is necessary to apply the following average after the Lagrangian hydrodynamic step:

$$\bar{y}_k = \frac{\sum_j^{N_{c,k}} y_{k,j} V_j}{\sum_j^{N_{c,k}} V_j} \quad \text{for } y \in \{\rho, u\} \text{ and } k \in \{f, p\}. \quad (24)$$

The fuel and pusher kinetic energies are computed as:

$$K_k = \frac{1}{2} \sum_j^{N_{c,k}+1} m_{F,j} v_j^2 \quad \text{for } k \in \{f, p\}, \quad (25)$$

with no need to hypothesise a velocity profile for the fuel as done for the Hydro I model. Finally, the surface velocities are simply  $v_1 = v_{N_{c,f}+1}$  and  $v_2 = v_{N_c+1}$ .

## 2.2. Thermal equilibration

The differential heating resulting from the operators described above leads to temperature separation between the electrons and ions (a single temperature is assumed for all ion species) in the fuel, which will be equilibrated over time through energy exchange due to inter-particle collisions and interactions with the mean field. For the single-fluid description adopted in **FLAIM** (as well as in our hydrodynamics codes) the rates of change of the internal energy densities are given by

$$\frac{du_i}{dt} = \dot{Q}_{ie}, \quad (26)$$

$$\frac{du_e}{dt} = \dot{Q}_{ei}. \quad (27)$$

The volumetric energy exchange rates,  $\dot{Q}_{ie} = -\dot{Q}_{ei}$ , can be evaluated in-line or by interpolation on pre-computed tables based on a variety of models. The standard model used in **FLAIM** is the reduced Fermi golden rule (RFGR) approach [18, 19], which compares well to Molecular Dynamics (MD) simulations for simple materials such as DT under the conditions of interest [20, 21].

Non-ideal effects such as large-angle binary collisions [22], local field corrections [23, 24] and the coupled mode effect [25, 26, 27, 28] are not important for the conditions achieved in burning fusion plasmas.

### 2.3. Wall

Heat losses from the fuel to the pusher are mediated by the presence of a *wall* (i.e., the fuel-pusher interface). The temperature difference between the fuel and the wall governs the heat losses, namely thermal conduction and radiation loss. The temperature of the wall is determined by a steady-state balance of the heat fluxes  $F(t)$  from the fuel (radiation, conduction and  $\alpha$  particles) and the flux diffused into the pusher,

$$F(t) = -\frac{4}{3} \frac{1}{\chi} \frac{\partial \sigma T_p^4}{\partial x} \Big|_{x=0}, \quad (28)$$

where  $\sigma$  is the Stefan-Boltzmann constant and  $\chi$  is the material opacity. The flux on the right-hand side is transported into the pusher by diffusion assuming local supersonic conditions (i.e., no convection). Therefore, the temperature gradient in Equation 28 is provided by the 1D planar diffusion equation

$$\frac{\partial u_p}{\partial t} = \frac{4}{3} \frac{\partial}{\partial x} \left( \frac{1}{\chi} \frac{\partial \sigma T_p^4}{\partial x} \right). \quad (29)$$

The solution of Equation 29 (using Equation 28 as time-varying boundary condition and an appropriate EoS for the pusher,  $\mathcal{F}_p(\rho_p, u_p, p_p) = 0$ ) provides the wall temperature:

$$T_w(t) = T_p(x, t) \Big|_{x=0}. \quad (30)$$

Since **FLAIM** is a reduced model, we seek a simplified approach to the numerical solution of Equation 29, that possibly removes any information of the spatial coordinates. The works of Hammer et al. [29] and Dodd et al. [9], present an approximate approach for deriving the wall temperature  $T_w$  and the position of the heat front  $x_F$  (with respect to the wall) in terms of simple time-dependent ODEs, assuming an infinitely steep front for the advancing heat wave, and a power-law form for the pusher EoS. In our work, the coefficients for the power-law EoS are calculated by a least-squares fitting over a prescribed region of the tabulated EoS for the pusher material. The pusher opacity is calculated using the **SpK** code [30]. We direct readers to the

reference works for more details about the derivation, implementation and verification of the model.

#### 2.4. Thermal conduction

Thermal conduction is accounted for following

$$\frac{du_k}{dt} = -\dot{Q}_{k,\text{cond}}, \quad (31)$$

where the conductive power density term is approximated as

$$\begin{aligned} \dot{Q}_{k,\text{cond}} &= \\ &= \frac{1}{V_f} \int_{V_f} \nabla \cdot (\kappa_k \nabla T_k) dV_f \\ &= \frac{1}{V_f} \int_{S_1} \kappa_k \nabla T_k \cdot \hat{\mathbf{n}} dS_1 \cong \kappa_k \frac{T_k - T_w}{R_1} \frac{S_1}{V_f} \end{aligned} \quad (32)$$

for  $k \in \{i, e\}$ , accounting for ion and electron conduction, and where a linear temperature profile is assumed in the fuel. A flux-limiter based on the particle thermal speed  $v_{\text{th}}$  is applied to avoid the inadequacy of the classic Fourier form of the thermal flux in the vicinity of steep spatial gradients [31],

$$\dot{Q}_{k,\text{cond}} = \min \left( \dot{Q}_{k,\text{cond}}, \beta_k v_{\text{th},k} u_k \frac{S_1}{V_f} \right), \quad (33)$$

where the coefficient  $\beta_k = 0.5, 0.05$  for ions and electrons respectively. Work is presently underway to develop a reduced kinetic description of the heat flux due to ions [32], the effects of which we will examine in a dedicated forthcoming publication. The total conductive power density is finally applied to the pusher to enforce energy conservation,

$$\frac{du_p}{dt} = \left( \dot{Q}_{i,\text{cond}} + \dot{Q}_{e,\text{cond}} \right) \frac{V_f}{V_p}. \quad (34)$$

For the thermal conductivity of the ions, we use Stanton and Murillo's result derived from the perturbative solution to the Boltzmann transport equation [33]. For the electrons, we use a modified version of Lee and More's simple relaxation time framework [34] corrected to account for electron-neutral and electron-electron collisions and suitable restrictions to the mean free path in the warm dense matter and solid phases. In both of the conductivities, the

appropriate effective ion charges are taken from the work of Hoffman et al. [35] for generalising the single-fluid framework to multi-component mixtures.

### 2.5. Radiation loss

The main mechanisms of electron-radiation interaction in the fuel are bremsstrahlung, Compton scattering and their inverse processes [8, 36, 37]:

$$\dot{Q}_{\text{brem}} = \nu_c n_e \frac{4}{\pi^{3/2}} Z_{\text{eff}} \frac{k_C e^2}{\hbar c} \sqrt{\frac{k_B T_e m_e c^2}{2}} I_B \left( \frac{T_r}{T_e} \right), \quad (35)$$

$$\dot{Q}_{\text{scatt}} = 4\nu_c u_r k_B \frac{T_e - T_r}{m_e c^2}, \quad (36)$$

where  $k_B$  and  $k_C$  define the Boltzmann and Coulomb constants respectively,  $\nu_c$  is the basic frequency for Compton scattering and  $I_B(x) = 2R(x)$ , with  $R(x)$  defining the regular Hurwitz integral [38]. These sources set the radiation energy density  $u_r$  in the fuel cavity. The expression for  $\dot{Q}_{\text{brem}}$  is augmented accounting for the fuel optical-depth following the work from Dodd et al. [9]. The radiation flux leaving a spherical cavity containing a radiative energy density  $u_r$  is  $u_r c/4$ , whilst the radiation flux emitted from the wall to the fuel (assuming a black-body) is  $\sigma T_w^4$ . The net radiative flux leaving the fuel volume is therefore:

$$\dot{Q}_{\text{rad}} = \left( u_r \frac{c}{4} - \sigma T_w^4 \right) \frac{S_1}{V_f}. \quad (37)$$

These source terms are applied to the relevant energy densities as

$$\frac{du_e}{dt} = -\dot{Q}_{\text{brem}} - \dot{Q}_{\text{scatt}}, \quad (38)$$

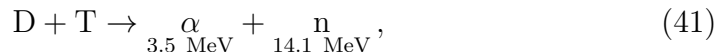
$$\frac{du_r}{dt} = \dot{Q}_{\text{brem}} + \dot{Q}_{\text{scatt}} - \dot{Q}_{\text{rad}}. \quad (39)$$

Finally, enforcing energy conservation for the whole system,

$$\frac{du_p}{dt} = \dot{Q}_{\text{rad}} \frac{V_f}{V_p}. \quad (40)$$

## 2.6. Thermonuclear burn

The thermonuclear burn includes the main branches of DT/DD reactions,



In a general reactive system including  $N_S$  species (6 in this case) and  $N_R$  reactions (3 in this case), one has to solve for the number density of each species  $j$ ,

$$\frac{dn_j}{dt} = s_j \sum_k^{N_R} \mathcal{R}_k \nu_{j,k} \quad \text{for } j = 0, \dots, N_S, \quad (44)$$

where  $s_j$  is the fraction of species  $j$  stopped in the fuel (if  $j$  is a product, otherwise  $s_j = 1$ ). For the  $\alpha$  particles,  $s_\alpha$  is provided by an alpha escape model such as Krokhin and Rozanov [39]. For neutrons, we assume complete escape  $s_n = 0$ .  $\nu_{j,k}$  is the stoichiometric coefficient of species  $j$  in reaction  $k$ . The reaction rates  $\mathcal{R}_k$  are based on the Bosch-Hale fits for the reactivities [40], with the option to use tabulated ones to account for the reactivity reduction due to Knudsen loss [41, 42]. The fuel internal energy density obeys

$$\frac{du_f}{dt} = \sum_i^{N_R} \mathcal{R}_i \sum_j^{N_{P,i}} K_{j,i} s_j, \quad (45)$$

in which  $K_{j,i}$  represents the kinetic energy of the product  $j$  in reaction  $i$ , scaled by the relative stopping fraction  $s_j$ , which is summed over the  $N_{P,i}$  products of reaction  $i$ . This rate is subsequently split into ion and electron contributions based on established models, such as those of Fraley et al. [43] or Atzeni and Caruso [44]. The fraction of each species  $j$  escaping the fuel is assumed to be entirely stopped by the pusher,

$$\frac{du_p}{dt} = \sum_i^{N_R} \mathcal{R}_i \sum_j^{N_{P,i}} K_{j,i} (1 - s_j). \quad (46)$$

Finally, the fuel mass density is re-evaluated based on the updated number densities  $n_j$  and the masses of the ions  $m_j$ ,

$$\rho_{\text{f}} = \sum_j^{N_{\text{S}}} n_j m_j, \quad (47)$$

from which fuel depletion naturally follows from the fact that  $n_{\text{n}}$  (neutron number density) is always null (since  $s_{\text{n}} = 0$ ).



### 3. Implementation

In this section we provide a brief description of how the model is numerically solved and an overview of the code structure and implementation.

#### 3.1. Numerical integration

The set of ODEs defining the mathematical model are solved with an operator-splitting approach, in order to efficiently handle the wide range of characteristic time-scales the different physical phenomena evolve on (e.g., very fast burn and relatively slow hydrodynamics). Given  $N_o$  physical operators (i.e., hydro, thermal conduction, radiation loss etc.), we can write

$$\mathbf{y}' = \mathbf{f}(\mathbf{y}', \mathbf{y}) = \sum_k^{N_o} \mathbf{f}_k(\mathbf{y}', \mathbf{y}) . \quad (48)$$

The numerical integration for each operator is based on a first-order explicit forward Euler, obtaining the following sequence for each time step  $\Delta t_0$ :

$$\begin{cases} \mathbf{y}_1^{n+1} = \mathbf{y}_0^n + \mathbf{f}_0(\mathbf{y}_0^n, \mathbf{y}_0^n) \Delta t_0 , \\ \mathbf{y}_2^{n+1} = \mathbf{y}_1^{n+1} + \mathbf{f}_1(\mathbf{y}_1^{n+1}, \mathbf{y}_1^{n+1}) \Delta t_0 , \\ \vdots \\ \mathbf{y}_{N_o}^{n+1} = \mathbf{y}_{N_o-1}^{n+1} + \mathbf{f}_{N_o-1}(\mathbf{y}_0^{n+1}, \mathbf{y}_0^{n+1}) \Delta t_0 , \end{cases} \quad (49)$$

where the subscripts  $i = 0, \dots, N_o$  identify the partial evolution of  $\mathbf{y}$  due to operator  $i$ . Equation 49 defines a Lie-Trotter splitting [45], since it involves a single forward Euler step using  $\Delta t_0$  for each operator. In **FLAIM** we also have the option of using a Strang splitting [46], in which the non-hydrodynamic physical operators are advanced for  $\Delta t_0/2$ , before and after the hydrodynamic one. We use Lie-Trotter splitting for most **FLAIM** simulation due to the lower computational cost, with Strang splitting only used in cases where extra time accuracy is required (Appendix B).

The inherent conditional stability of explicit schemes is satisfied by a sub-cycling methodology. The first operator  $\mathbf{f}_0$  is the hydrodynamics, employing a time step  $\Delta t_0$ , and different time steps  $\Delta t_k$  are used for the remaining  $\mathbf{f}_k$  operators, either based on their specific stability conditions or determined by imposing a specific requirement for the solution at the next step (e.g., setting a maximum fractional change of one or more variables). If  $\Delta t_k < \Delta t_0$ , the

operator  $\mathbf{f}_k$  is internally evolved multiple times until  $\sum_j \Delta t_{j,k} = \Delta t_0$ , otherwise  $\Delta t_0$  is used<sup>5</sup>. The hydro time step  $\Delta t_0$  is computed for the model Hydro I (Table 1) as

$$\Delta t_0 = \eta \frac{R_1}{v_1}, \quad (50)$$

with  $\eta$  is a user-specified safety factor (usually  $0.01 \leq \eta \leq 0.001$ ). For the Hydro II model,  $\Delta t_0$  is based on the classic Courant–Friedrichs–Lewy (CFL) condition

$$\Delta t_0 = a \min \left( \frac{\Delta x_j}{|v_j + c_{s,j}|} \right) \quad \text{for } j = 0, \dots, N_c, \quad (51)$$

where  $v_i$  is the cell-centred (linearly interpolated) grid velocity and  $c_{s,i}$  is the local sound speed, extracted from the EoS table. The Courant number  $a$  is typically chosen to be  $0.1 \leq a \leq 0.5$ .

### 3.2. Code structure

FLAIM is developed as a stand-alone library written entirely in C++. The code core is characterised by a modular structure, in order to provide a versatile tool that allows developers to easily implement and switch between models with minimal effort. To this purpose, FLAIM heavily relies on the object-oriented features of the C++ language for the implementation of the physical operators. This allows the users to easily implement various time integration methods or different versions of the same operator, and to test them rapidly without changing any aspect about the general code structure.

The FLAIM external API is written in Python, using the `Boost.Python` library to enable the interoperability between the two programming languages. This has multiple advantages, including a facilitated interaction with a user-friendly language, immediate post-processing capabilities, an extra layer of control on the functionality exposed to the API (in addition to the encapsulation provided by C++), as well as the complete separation between interface and implementation.

---

<sup>5</sup>The subscript  $j$  for the internal time steps  $\Delta t_{j,k}$  is justified by the fact that they can potentially change at every sub-step.

	Revolver [2]	B2 scan	n points
$R_1$ [ $\mu\text{m}$ ]	326	150 – 450	5
$\Delta_p$ [ $\mu\text{m}$ ]	60	30 – 100	5
$v$ [km/s]	200	100 – 300	5

Table 2: Parameter space explored by the B2 simulation scan (125 simulations, for each coordinate the n points are equidistant) in terms of initial fuel radius  $R_1$ , initial pusher thickness  $\Delta_p$  and initial implosion velocity  $v = v_1 = v_2$ . Revolver parameters are reported for reference. B2 simulations are run with a resolution of  $\sim 0.6 \mu\text{m}/\text{cell}$  based on a standard convergence analysis.

#### 4. Comparison with 1D hydrodynamic simulations

To use FLAIM as an efficient and reliable surrogate for exploring and for optimising target designs, one must assess its accuracy in a wide region of the design space with respect to well-established high fidelity models. In this section we focus on the analysis of the hydrodynamic operator<sup>6</sup> (Table 1).

At FLF we have developed a suite of numerical capabilities to support our experimental activity and design work, including a Resistive-Magneto-Hydrodynamic (RMHD) code called B2. We refer to Appendix C for a brief description of the B2 code, as well as for a list of verification test cases for the principal operators/models relevant for this work.

##### 4.1. Simulation scan

In order to quantify the physical accuracy of FLAIM against B2, a quantitative comparison over a large parameter space holds the utmost importance. We have run a scan of 125 1D spherical B2 simulations that represent variations of the Revolver design point [2]. The pusher material is gold ( $\rho_p = 19.3 \text{ kg/m}^3$ ) and the fuel is an equimolar mixture of DT at  $T_i = T_e = 33 \text{ K}$ , with an initial density of  $\rho_f = 0.173 \text{ kg/m}^3$ . The B2 simulations are initialised with a flat velocity profile in the pusher and  $p_{N_c+1} = 0$  outside the capsule. Table 2 summarises the parameters defining the scan.

---

<sup>6</sup>The simulations showed in this Section were conducted with thermal equilibration for both codes (Equations 26, 27), to avoid the preferential heating of any component of the fluid.

FLAIM and B2 will be compared based on the profiles of volume-averaged conserved quantities. Whilst these are naturally captured in FLAIM (see Section 2), they must be explicitly post-processed from 1D B2 simulations. For a generic quantity  $y_{\text{B2}}$ , we have for the fuel

$$\bar{y}_{\text{B2,f}}(t) = \frac{3}{R_1^3} \int_0^{R_1} r^2 y_{\text{B2}}(t, r) \, dr, \quad (52)$$

whereas for the pusher we can write

$$\bar{y}_{\text{B2,p}}(t) = \frac{3}{R_2^3 - R_1^3} \int_{R_1}^{R_2} r^2 y_{\text{B2}}(t, r) \, dr, \quad (53)$$

where  $y \in \{u, \rho\}$ , i.e. the conserved quantities defining the system. The average profiles for temperature  $\bar{T}_{\text{B2},k}(t)$  and pressure  $\bar{p}_{\text{B2},k}(t)$  for  $k \in \{\text{f}, \text{p}\}$  are derived from the fuel and pusher equations of state, which are the same for the two codes. The comparison metric is an  $L_2$  norm for the fuel ion temperature  $T_i(t)$  and mass density  $\rho_f(t)$  temporal profiles, defined as

$$L_2(y) = \sqrt{\sum_i^{N_{\text{steps}}} \left( \frac{y_{\text{FLAIM}}(t_i) - \bar{y}_{\text{B2}}(t_i)}{\bar{y}_{\text{B2}}(t_i)} \right)^2} \quad \text{for } y \in \{T_i, \rho_f\}, \quad (54)$$

where  $y$  is the temporal profile of the physical quantity of interest and  $N_{\text{steps}}$  is the number of time steps of the simulation. This norm measures the average distance between the profiles predicted by FLAIM and B2 and provides a metric to quantify the agreement between the two codes.

#### 4.2. Hydro I

We report here a brief description of how the scan defined in Table 2 is run using the model Hydro I (Table 1), based on the assumption of a spatially uniform velocity profile in the pusher (Equation 19). As reported in several works [2, 4], the implosion dynamics can be split in two different phases: (i) a shock-heating phase, which lasts until the initial shock reaches the origin; (ii) a quasi-isentropic compression phase that brings the fuel state towards the ignition conditions. The fuel energy equation for Hydro I in FLAIM (Equation 12) describes an adiabatic compression of a generic volume  $V_f$ . This means that with FLAIM we are only able to describe the *second* phase of the implosion dynamics, due to the lack of shock description in volume-averaged hydrodynamics. Therefore, for each B2 simulation:

1. We identify the time  $t_{\text{ws}}$  (warm-start) at which the initial shock reaches the origin and reflects back intersecting the fuel-pusher interface<sup>7</sup>, and extract the fuel and pusher states (in terms of volume-averaged  $\rho, u$  and the pusher kinetic energy  $K_p$ ) and geometry ( $R_1, R_2, \Delta_p$ ) at  $t_{\text{ws}}$ ;
2. This intermediate configuration is used to initialise a FLAIM simulation and to run it until completion ( $t = t_{\text{end}}$ );
3. Using the metric defined in Equation 54, the B2 and FLAIM outputs are compared for  $t_{\text{ws}} \leq t \leq t_{\text{end}}$ .

### 4.3. Hydro II

Using the model Hydro II, the condition of quasi-isentropic transformation is not required: the fluid elements are still described by an quasi-isentropic transformation, but the presence of artificial viscosity allows us to track the shock propagation, as well as stabilising the numerical solution [17]. This makes the model Hydro II suitable for the modelling of both phases of the implosion dynamics, allowing us, in principle, to compare the FLAIM and B2 directly from cold conditions. However, to maintain consistency with the approach used for the model Hydro I and to provide a solid comparison based on *equivalent* initial conditions, we performed the scan following the steps 1 – 3 defined in Section 4.2 (i.e., starting from  $t_{\text{ws}}$ ). The comparison is still based on the  $L_2$  norm defined in Equation 54.

### 4.4. Quantitative comparison: $L_2$ norms

Figure 3 reports the  $L_2$  norms for ion temperature  $T_i$  and mass density  $\rho_f$  in the fuel for the scan using Hydro I, as a function of the initial fuel radius  $R_1$  at different initial implosion velocities  $v$  and pusher thicknesses  $\Delta_p$ . One immediately notices a common behaviour of the  $L_2$  norm in the parameter space: (i) it decreases with the initial fuel radius  $R_1$ , (ii) it increases with the initial pusher thickness  $\Delta_p$  and (iii) it is weakly dependent on the initial implosion velocity  $v$ .

In contrast, the  $L_2$  norm profiles provided by Hydro II (Figure 4), show significant differences. First, the average magnitude of the  $L_2$  norm has considerably decreased (by a factor of  $\sim 10 - 40$ ), especially for the density

---

<sup>7</sup>The actual definition of shock-heating phase given by Molvig [2] limits the dynamics until the shock converges on the origin. We decided to extend it to allow the residual weak shocks to reverberate and adhere more stringently to the adiabatic compression requirement that FLAIM necessitates.

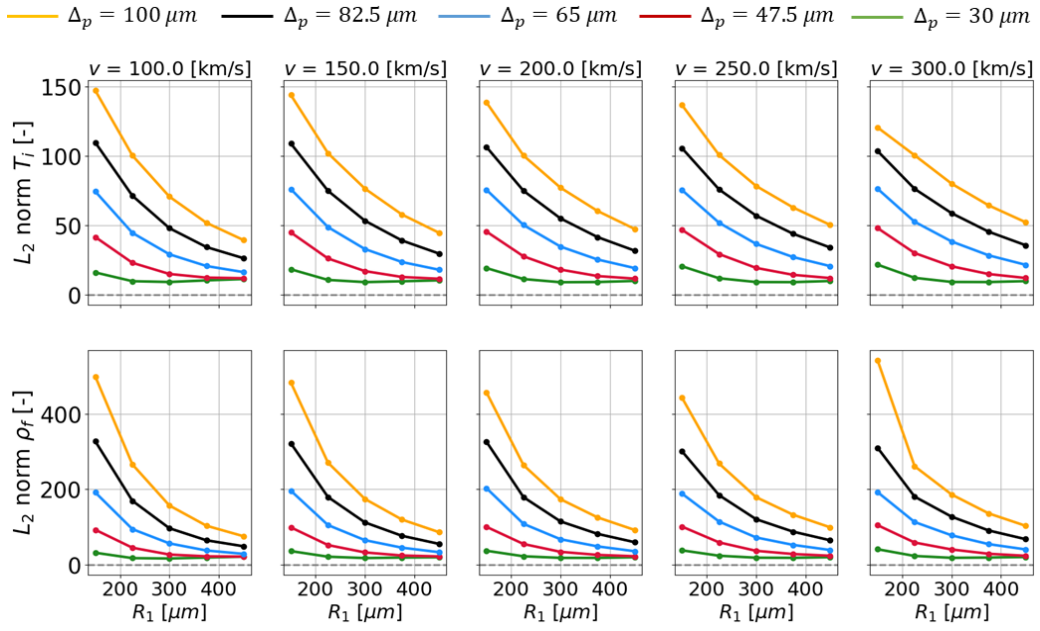


Figure 3:  $L_2$  norms (Equation 54) for the comparison B2-FLAIM for the fuel ion temperature  $T_i$  (top row) and mass density  $\rho_f$  (bottom row) profiles at different initial fuel radii  $R_1$ , pusher thicknesses  $\Delta_p$  and implosion velocities  $v$ . Hydro I model (Table 1).

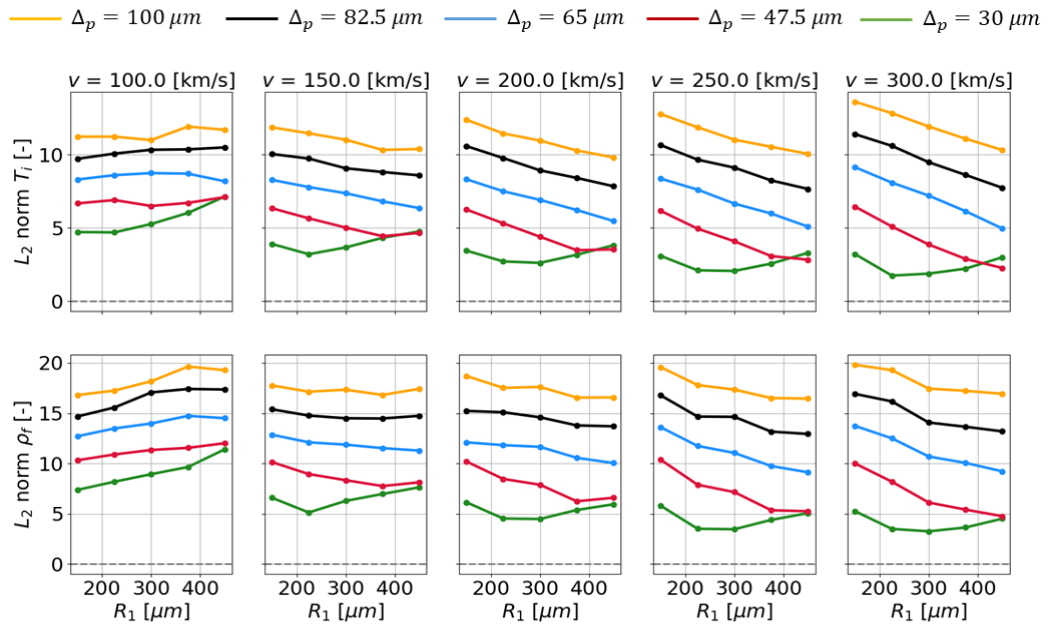


Figure 4:  $L_2$  norms (Equation 54) for the comparison B2-FLAIM for the fuel ion temperature  $T_i$  (top row) and mass density  $\rho_f$  (bottom row) profiles at different initial fuel radii  $R_1$ , pusher thicknesses  $\Delta_p$  and implosion velocities  $v$ . Hydro II model (Table 1).

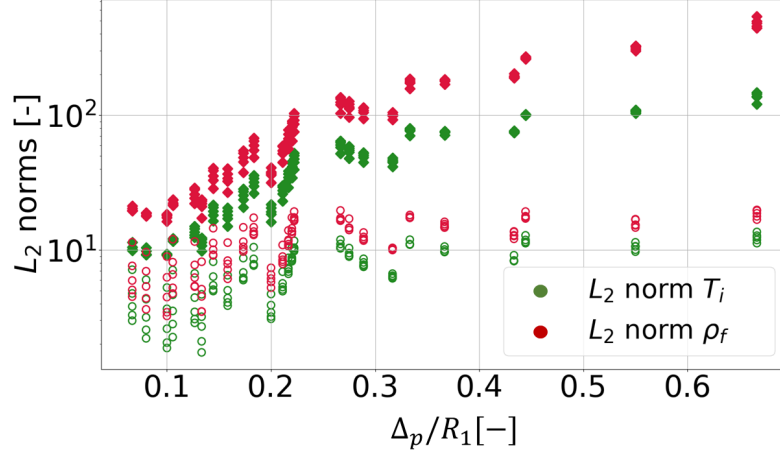


Figure 5: Scatter plot of  $L_2$  norms of the ion temperature  $T_i$  and fuel density  $\rho_f$  vs.  $\Delta_p/R_1$  for the scan defined in Table 2. Diamonds for the model Hydro I, empty circles for the model Hydro II.

profile, denoting a much better agreement between the profiles. Secondly, the strong variation with respect to  $R_1$  and  $\Delta_p$  is no longer visible, and a very weak dependence is observed. This aspect is further exemplified by the scatter plot of the values of  $L_2$  norms in function of the  $\Delta_p/R_1$  ratio (Figure 5) for the two hydro models Hydro I and Hydro II. We can observe an exponential dependence for the model Hydro I, in which the accuracy of FLAIM with respect to an equivalent B2 simulation rapidly worsens for increasing values of the  $\Delta_p/R_1$  ratio, i.e. for relatively thick pushers. Conversely, for the model Hydro II the correlation between the  $L_2$  norm and the ratio  $\Delta_p/R_1$  is nearly disappeared. The residual error cannot be clearly ascribed to a specific aspect of the modelling, but it is most likely a combination of the intrinsic differences between FLAIM and B2 (e.g., bulk vs. local thermal equilibration, type of discretisation, numerical schemes).

#### 4.5. Qualitative comparison: temporal profiles

Whilst the analysis of the  $L_2$  norms can give us a quantitative idea of the average distance between the profiles predicted by FLAIM and B2, the difference is well-demonstrated by some selected simulations. We have chosen three points out of the original parameter scan:

- Case 1:  $R_1 = 450 \mu\text{m}$ ;  $\Delta_p = 30 \mu\text{m}$ ;  $v = 200 \text{ km/s}$ ;



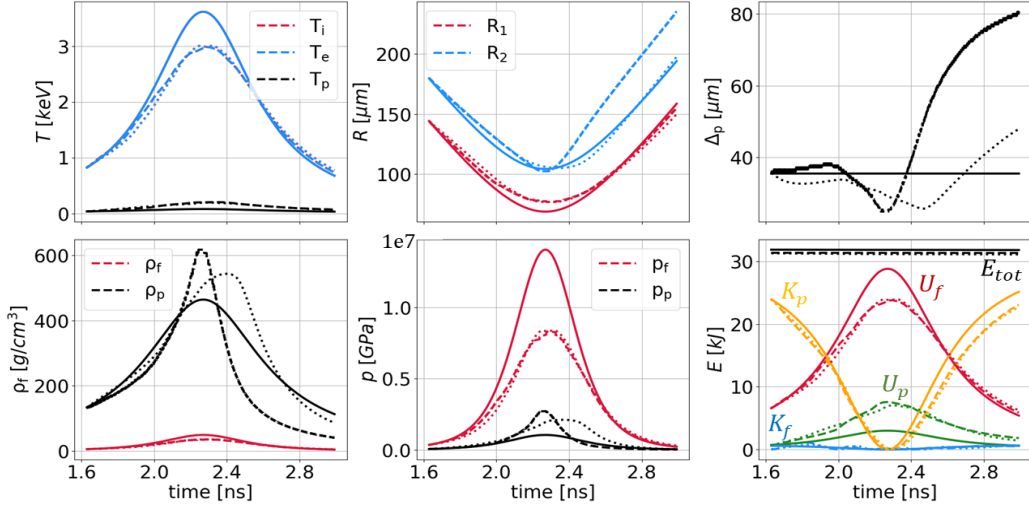


Figure 6: Temporal profiles of temperatures  $T_i, T_e, T_p$ , radii  $R_1, R_2$ , pusher thickness  $\Delta_p$  (top row). Fuel and pusher densities  $\rho_f, \rho_p$ , pressures  $p_f, p_p$ , and energy contributions (kinetic  $K_i$ , internal  $U_i$ , total  $E_{\text{tot}} = \sum_i U_i + K_i$ , for  $i \in \{f, p\}$ ) (bottom row). Solid line is FLAIM with model Hydro I, dotted line is FLAIM with model Hydro II, dashed line is B2. Case 1.

- Case 2:  $R_1 = 300 \mu\text{m}$ ;  $\Delta_p = 65 \mu\text{m}$ ;  $v = 200 \text{ km/s}$ ;
- Case 3:  $R_1 = 150 \mu\text{m}$ ;  $\Delta_p = 100 \mu\text{m}$ ;  $v = 200 \text{ km/s}$ .

These cases are shown in Figures 6, 7, 8, comparing the temporal profiles of key physical quantities for B2 (dashed line) vs. FLAIM using the model Hydro I (solid line) and Hydro II (dotted line). The most evident aspect to notice (for all cases) is that the pusher thickness predicted by B2 strongly deviates from the constant profile assumption underlying the Hydro I model, particularly for thick pushers: the shell actually undergoes a significant compression during the implosion phase, followed by a strong expansion after stagnation. Elucidation of the origin of this behaviour is provided by examination of the evolution of the energetics in Figure 8. A clear correlation between the internal energy of the fuel and kinetic energy of the pusher can be seen for the Hydro I model, indicating that the latter is almost entirely used to compress the capsule. The same profiles predicted by B2 are qualitatively different: in this case, a significant fraction of the pusher kinetic energy is consumed to compress the pusher *itself*, leaving only a minor contribution for the fuel compression. This explains why Hydro I tends to grossly over-predict the  $p dV$

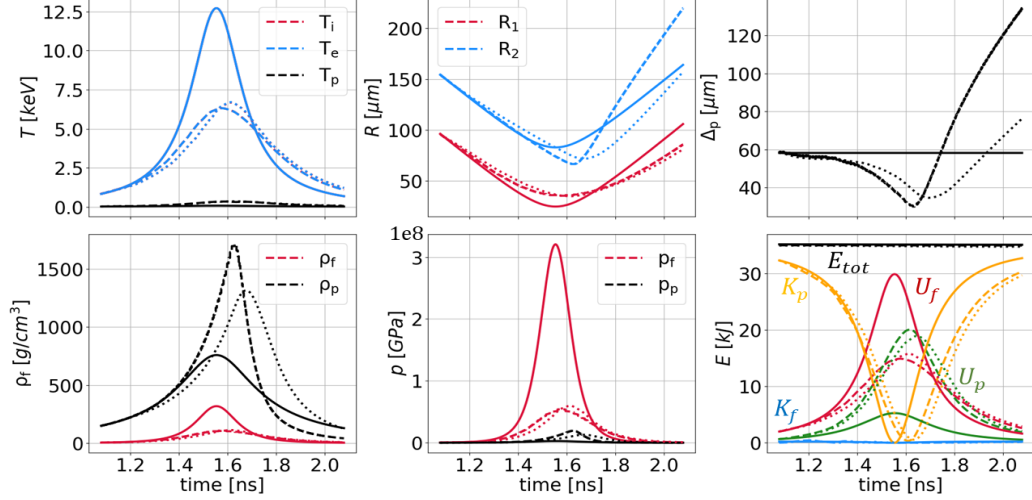


Figure 7: Temporal profiles of temperatures  $T_i, T_e, T_p$ , radii  $R_1, R_2$ , pusher thickness  $\Delta_p$  (top row). Fuel and pusher densities  $\rho_f, \rho_p$ , pressures  $p_f, p_p$ , and energy contributions (kinetic  $K_i$ , internal  $U_i$ , total  $E_{\text{tot}} = \sum_i U_i + K_i$ , for  $i \in \{f, p\}$ ) (bottom row). Solid line is FLAIM with model Hydro I, dotted line is FLAIM with model Hydro II, dashed line is B2. Case 2.

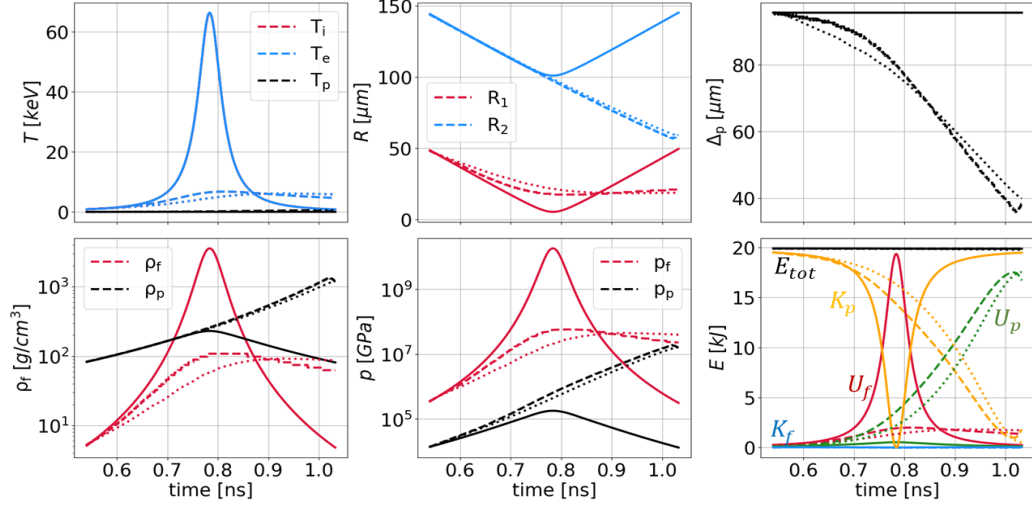


Figure 8: Temporal profiles of temperatures  $T_i, T_e, T_p$ , radii  $R_1, R_2$ , pusher thickness  $\Delta_p$  (top row). Fuel and pusher densities  $\rho_f, \rho_p$ , pressures  $p_f, p_p$ , and energy contributions (kinetic  $K_i$ , internal  $U_i$ , total  $E_{\text{tot}} = \sum_i U_i + K_i$ , for  $i \in \{f, p\}$ ) (bottom row). Solid line is FLAIM with model Hydro I, dotted line is FLAIM with model Hydro II, dashed line is B2. Case 3.

work on the fuel and this is visible from the fuel radius  $R_1$  profile, as well as the fuel density  $\rho_f$ , pressure  $p_f$  and temperature  $T_f$  in Figures 7, 8. Forcing the imploding shell to maintain a constant thickness puts a severe limit to its compressibility, leaving a kinetic energy reservoir that is inevitably spent on the capsule compression. This phenomenon is less evident for thin shells, but has a strong impact for thicker pushers (in Figure 8,  $\Delta_p^{\min}/\Delta_p^0 \approx 0.5$ ) leading to the conclusion that, whilst the assumption of constant thickness can be reasonable for thin pushers, it rapidly breaks down for thicker ones. This is the same issue encountered for the very simplistic model Hydro 0 (Table 1), and it demonstrates that even an improved model adopting a constant-thickness compressible pusher is still far from accurate. A similar conclusion has been reached by previous works [13, 14] in the context of hot-spot ignition regarding the inadequacy of incompressible thin shell models (equivalent to the model Hydro 0). The model Hydro I describes an intermediate situation (a pusher with *limited* compressibility), but the physical interpretation is analogous.

Analysing the results from Hydro II, we can see that the fuel compression is described much more accurately. The profiles show good agreement with respect to B2. The pusher thickness profiles predicted by FLAIM follow the B2 ones very closely, exhibiting a major compression during the implosion, particularly for thick pushers. The shell compression occurs at the expense of its own kinetic energy, which leaves less margin to compress the fuel. The energy distribution between fuel and pusher is also correctly predicted. An alternative way to interpret these results focuses on the shock propagation in the pusher. Whilst for thin shells the information is rapidly propagated between the inner and the outer surface, thick shells require more time for this to occur. This leads to a *reduced* compressive work on the fuel provided only by the shocked region of the pusher. Moreover, thick shells are also characterised by a strong pressure gradient [3] (directed inwards), which further contributes to the pusher deceleration. Differently from the Hydro I model, the Hydro II model naturally describes the radial pressure profile and is capable of tracking shocks in the materials (Section 2), capturing this dynamics correctly.

## 5. Comparison with 1D fully-integrated physics simulations

In the previous section we analysed in detail the level of accuracy of the hydrodynamics implemented in FLAIM, finding that the approximation of a flat velocity profile in the pusher (i.e., constant thickness) had a detrimental impact on the fidelity of the compression physics. In this section, we present a comparison with B2 for burning fuel capsules, to investigate the actual impact that an incorrect treatment of the compression dynamics has on the ignition and burn physics of the target. The scan defined in Table 2 is defined as a fully-integrated physics scan, i.e., run activating the burn operator and the heat losses (conduction and radiation) for both FLAIM and B2. The electron-ion split-factor is based on the Fraley’s model [43] for both codes. The  $\alpha$  particle escape fraction in FLAIM is based on the model of Khrokhin and Rozanov [39], whilst in B2 it is naturally accounted for solving a diffusion equation for the  $\alpha$  particle transport [47].

Instead of relying on  $L_2$  norms, the comparison in this case is carried out in terms of heatmaps of key burn properties of interest to determine the target performance, namely the final neutron yield  $E_n$  and the deuterium burn fraction  $\Phi_D$ , respectively defined as

$$E_n = \sum_i^{N_R} \mathcal{R}_i K_{n,i}, \quad (55)$$

$$\Phi_D = 1 - \frac{n_D}{n_D^0}. \quad (56)$$

Figures 9 and 10 report the surfaces of  $E_n$  and  $\Phi_D$  in the parameter space predicted by FLAIM with Hydro I (top row), FLAIM Hydro II (middle row) and B2 (bottom row).

The B2 maps show a distinct separation between a non-burning region and a strongly burning region, in which the separatrix (white dashed line) identifies the iso-contour corresponding to  $\Phi_D = 0.05$ . This line can be interpreted as the minimum implosion velocity  $v^*$  (function of  $R_1, \Delta_p$ ) required to ignite and burn a significant fraction of the fuel. The choice of using a  $\Phi_D$  iso-contour was motivated by the fact that we found the volume ignition criterion by Molvig et al. [2] (Equation 57) to be insufficient for defining sensible separatrices in the maps. In particular, Equation 57 labels as igniting *all* the simulations of the scan (Table 2). While we recognise the intention behind this criterion is to identify the moment of upstream ignition

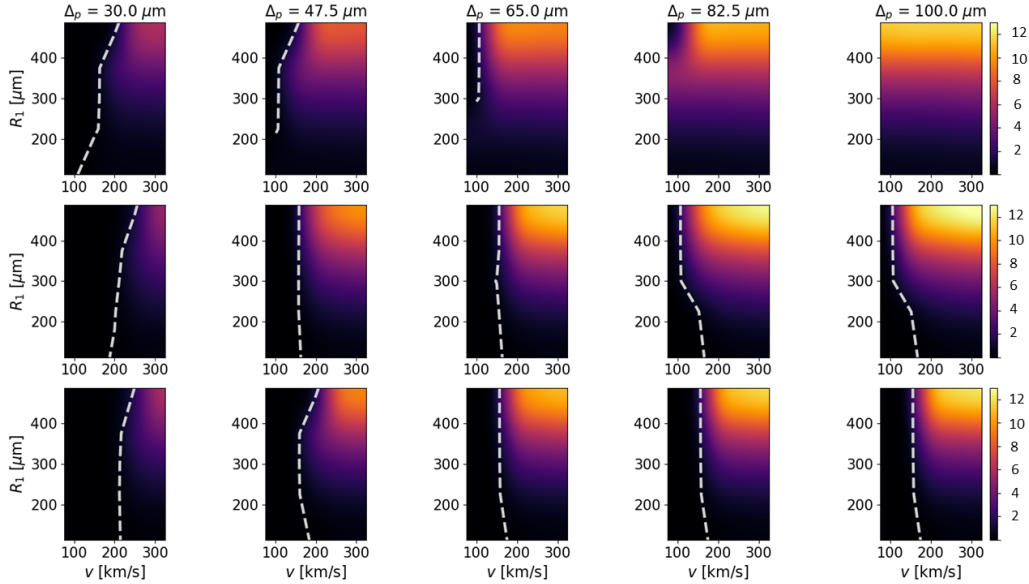


Figure 9: Heatmaps of final neutron yield  $E_n$  [MJ] for the simulation scan defined in Table 2. Hydro I FLAIM (top row), Hydro II FLAIM (middle row) and B2 (bottom row). The dashed lines indicate the iso-contour of constant burn fraction  $\Phi_D = 0.05$ .

for a sans-losses implosion (like Revolver), it ultimately fell short in effectively distinguishing between igniting and non-igniting regions within the parameter space. Hence, the choice to adopt a simple  $\Phi_D = 0.05$  iso-contour, representing  $\sim 1/10$  of the fuel burn fraction of Revolver [3]. Given the steep gradient of the surface  $\Phi_D(R_1, v, \Delta_p)$  (characteristic of ignition phenomena), no noticeable change in the separatrix position was observed when varying the iso-contour value within the range  $\{0.01 - 0.15\}$ .

Looking at the B2 maps (bottom row), for thin shells,  $v^*$  tends to decrease with the pusher thickness (from  $\sim 210$  km/s for a  $30 \mu\text{m}$  pusher to  $\sim 180$  km/s for a  $65 \mu\text{m}$  pusher), which can be explained by the higher kinetic energy available to compress the fuel. However, a plateau is visible for  $\Delta_p \gtrsim 65 \mu\text{m}$ : further thickening the pusher after this point does not change the ignition requirements in terms of implosion velocity. This means that the target is able to convert only a fraction of the pusher kinetic energy to fuel internal energy and the rest is simply taken up by the shell self-compression. In the same region ( $\Delta_p \gtrsim 65 \mu\text{m}$ ), whilst the neutron yield (Figure 9) increases with the capsule size (because more fuel is available), the final burn fraction (Figure 10) is roughly independent of it.

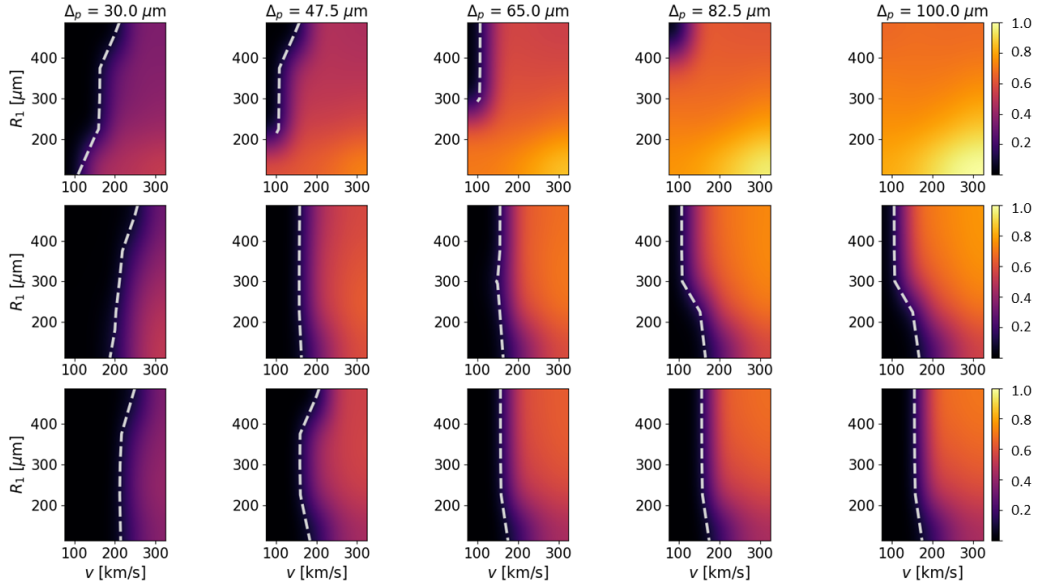


Figure 10: Heatmaps of final deuterium burn fraction  $\Phi_D$  for the simulation scan defined in Table 2. Hydro I FLAIM (top row), Hydro II FLAIM (middle row) and B2 (bottom row). The dashed lines indicate the iso-contour of constant burn fraction  $\Phi_D = 0.05$ .

FLAIM run with Hydro II (middle row) generally compares well with B2: the lines representing  $v^*$  are in good agreement and clearly separate two similar regions of the parameter space. For thicker pushers, FLAIM exhibits a more pronounced dependence on  $R_1$ , whereas B2 provides a quasi-vertical separatrix. As reported in Section 5.1, this is attributable to the simplified thermal conduction model, that tends to overestimate the heat losses at small fuel radii (Equation 32). Both the neutron yield and the burn fraction are in good agreement, even though slightly overestimated, especially at high implosion velocity. Finally, FLAIM tends to underevaluate  $v^*$  for thicker pushers, showing a premature ignition with respect to B2. Overall, the comparison is satisfactory, showing that FLAIM can predict with sufficient accuracy the ignition surfaces in the parameter space when adopting the model Hydro II for the hydrodynamics.

Conversely, the heatmaps predicted using the model Hydro I (top row) are qualitatively different. The comparison is acceptable for very thin pushers, but rapidly worsens for thicker ones. In particular, for  $\Delta_p \geq 82 \mu\text{m}$  the strongly-burning region covers almost the whole parameter space, with unrealistic burn fractions up to  $\Phi_D \approx 1$  predicted. This behaviour is a con-

	B2 scan	n points
$R_1$ [ $\mu\text{m}$ ]	150 – 450	10
$\Delta_p$ [ $\mu\text{m}$ ]	82.5 – 100	3
$v$ [km/s]	100 – 300	10

Table 3: High-resolution B2 simulation scan (300 simulations, for each coordinate the n points are equidistant) in terms of initial fuel radius  $R_1$ , initial pusher thickness  $\Delta_p$  and initial implosion velocity  $v = v_1 = v_2$ , defining a sub-region of the space in Table 2.

sequence of the incorrect description of the hydrodynamics resulting from assuming a constant thickness shell, that we extensively analysed in Section 4. The overestimation of the fuel compression has a direct impact on the burn physics due to its quadratic dependency on the mass density, leading to the misleading interpretation that thick pushers are more efficient in compressing the capsule because of their large kinetic energy. In reality, only a fraction of this kinetic energy can be effectively coupled to the the fuel, whilst the rest is actually spent for shell self-compression. Interestingly, the B2 maps show that this fraction is independent of the pusher thickness, and the FLAIM scan with Hydro II captures this behaviour. The tendency of the model Hydro I to predict ignition and strong burn in regions where higher-fidelity simulations fail to do so is insidious and the worst possible scenario for use in optimisations because it is fundamentally *optimistic*. Using a reduced model for large scans, one naturally expects some discrepancy in predicting ignition regions, but one would rather have a conservative version of it, in which ignition and burn are not predicted where they actually should be. This allows for the design and optimisation of experiments with some margin for the expected performance, even accounting for the inevitable uncertainties of a simplified modelling approach.

### 5.1. Analysis on the role of heat losses

Although we have demonstrated that the efficacy of FLAIM as a predictive surrogate using the model Hydro II, some discrepancies persist across the design space. Firstly, whilst the accuracy is satisfactory for small thickness pushers (and much more improved for thick ones), it is possible to observe a region ( $120 \text{ km/s} \lesssim v^* \lesssim 170 \text{ km/s}$ ) where FLAIM still incorrectly predicts ignition and burn. Secondly, even when both models roughly agree on the

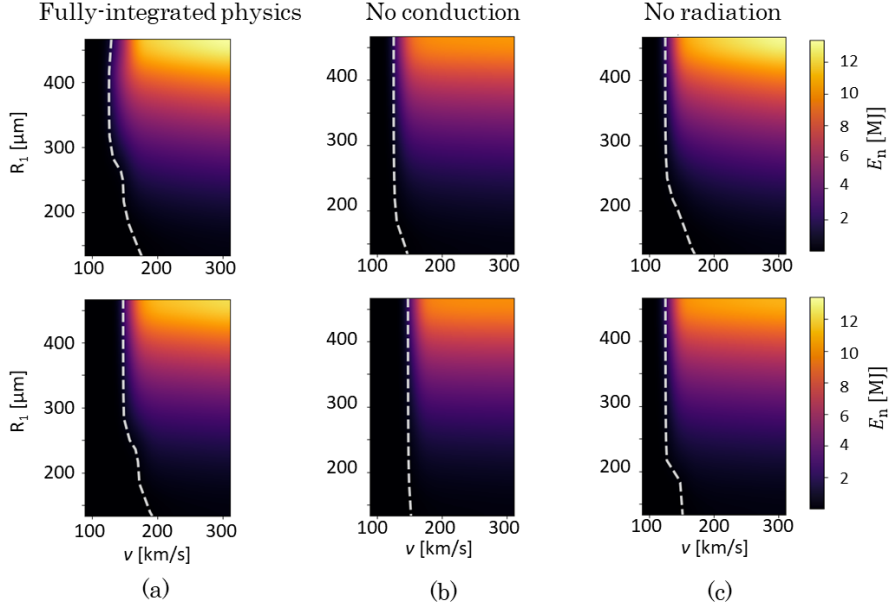


Figure 11: Heatmaps of neutron energy  $E_n$  for  $\Delta_p = 82.5 \mu\text{m}$  for fully-integrated physics simulations (a), without thermal conduction (b) and without radiation loss (c). FLAIM results (top row) vs. B2 results (bottom row). The dashed lines indicate the iso-contour of constant burn fraction  $\Phi_D = 0.05$ .

shape of the ignition region, FLAIM tends to slightly overpredict both neutron yield and burn fraction for thick pushers. To complete the analysis, it is worth investigating the reason behind these inconsistencies turning our attention to the heat loss mechanisms. As reported in Section 2, thermal conduction is implemented in a simplified manner (Equation 32), as well as the radiation loss (Equation 37). Moreover, the wall (which ultimately governs the temperature difference that drives the heat fluxes) is also modelled with a simplified approach to avoid the solution of diffusion equation (Equation 29). Heat losses play a key role in determining the ignition of the fuel capsule and, whilst their accurate modelling is (deliberately) out of the scope of a work on a simplified ignition model like FLAIM, it is valuable to analyse the impact that a simplified treatment has on the model accuracy.

To this purpose, we ran a B2 scan removing each heat loss mechanism independently to investigate their impact in isolation:

1. The first scan is run removing radiation loss, leaving only thermal conduction as the sole heat loss mechanism;



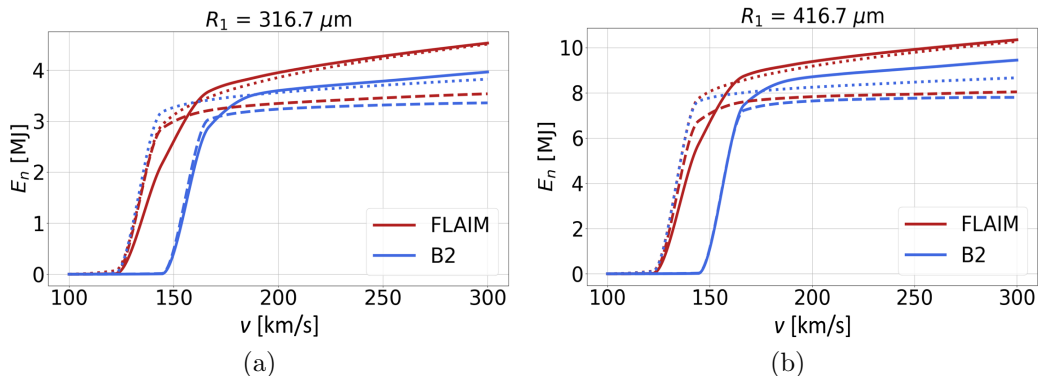


Figure 12: Profiles of neutron energy  $E_n$  along iso-lines of constant fuel radius  $R_1 = 316.7 \mu\text{m}$  (a) and  $R_1 = 416.7 \mu\text{m}$  (b) for the heatmap at  $\Delta_p = 82.5 \mu\text{m}$  (Figure 11). Full-physics (solid line), no-conduction (dashed line) and no-radiation (dotted line).

2. The second scan is run removing thermal conduction (both ion and electron), leaving only radiation loss as the sole heat loss mechanism.

Since thick pushers are most relevant for the discussion, we ran a scan in the sub-region  $82.5 \mu\text{m} \leq \Delta_p \leq 100 \mu\text{m}$ , increasing the resolution in terms of fuel radius  $R_1$  and implosion velocity  $v$  (from 5 to 10 points for each coordinate). The scan now includes 300 simulations in a sub-region of the parameter space defined in Table 2 and is summarised in Table 3. This scan is run for the three cases: (i) with all physical operators activated (i.e., hydrodynamics, burn, conduction, radiation)<sup>8</sup>; (ii) without thermal conduction (i.e., hydrodynamics, burn, radiation); (iii) without radiation loss (i.e., hydrodynamics, burn, conduction). Thermal equilibration and wall operators are always included. The hydrodynamic model is set to Hydro II (Table 1).

Figures 11 a, b, c report the neutron yield  $E_n$  maps for the three cases respectively, for FLAIM and B2 at  $\Delta_p = 82.5 \mu\text{m}$ . Both codes predict a lower neutron yield when heat losses are removed, due to the higher adiabat and the reduced compressibility of the fuel capsule. As previously discussed, the FLAIM scan presents two aspects of discrepancy with respect to B2. Firstly, a region of premature ignition ( $120 \text{ km/s} \lesssim v^* \lesssim 170 \text{ km/s}$ ) can be observed. At higher resolution, its width is slightly reduced ( $120 \text{ km/s} \lesssim v^* \lesssim$

<sup>8</sup>This scan was shown in Section 4, but it is run again at the same resolution defined in Table 3.

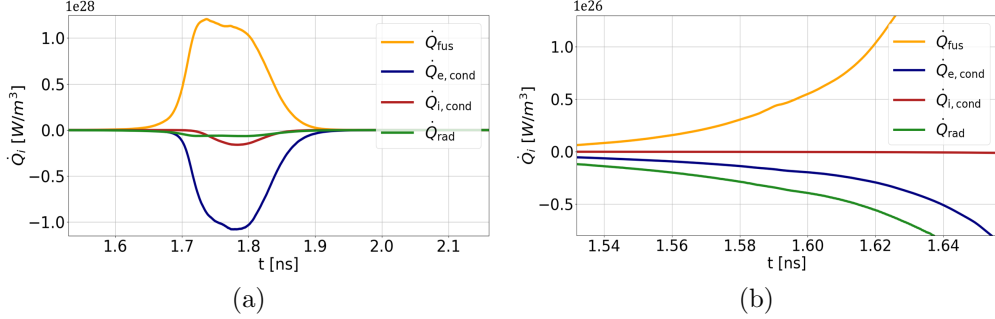


Figure 13: Plots of power density contributions (burn  $\dot{Q}_{\text{fus}}$ , electron conduction  $\dot{Q}_{\text{e,cond}}$ , ion conduction  $\dot{Q}_{\text{i,cond}}$  and radiation  $\dot{Q}_{\text{rad}}$ ) to the fuel internal energy density  $u_f$  for the Revolver design [2] simulated with FLAIM using Hydro II. Figure (b) reports a detail of Figure (a) in the range  $1.54 \lesssim t \lesssim 1.64$  ns, to highlight the implosion phase.

160 km/s), but still clearly visible. Secondly, a general overestimation of  $E_n$  for large capsule radii is noticeable. Analysing the map run without thermal conduction (b), one immediately notices that the agreement in terms of  $E_n$  between FLAIM and B2 is now excellent for  $v^* \gtrsim 160$  km/s. The dependency of  $v^*$  on  $R_1$  visible in the maps in Figure 11a has almost disappeared, providing a quasi-vertical separatrix for both codes. However, the spurious burning region ( $120 \text{ km/s} \lesssim v^* \lesssim 160 \text{ km/s}$ ) that was visible for the FLAIM scan in Figure 11a is still present. This leads to the conclusion that thermal conduction dominates the losses in the burning regime since most of the impact of its removal is localised in this region of the parameter space, affecting in a minor way the position of the separatrix.

This behaviour is confirmed analysing the scan in which radiation is removed from the system (c): in this case we observe the opposite scenario, in which the general overprediction of  $E_n$  in the burning regime remains unchanged, whilst  $v^*$  is now in good agreement to what predicted by B2 (with minor deviations at small radii due to the conduction model). This indicates that radiation loss is the main heat loss mechanism during the implosion phase (defining whether it would lead to ignition or not) and its removal allows us to accurately predict the location of the strong-burning region with respect to B2.

This can be more clearly observed in Figure 12, reporting the profiles of  $E_n$  in the velocity space for two selected radii from Figure 11 for the three cases (fully-integrated physics, no conduction, no radiation). The visible gap

in the implosion velocity required for ignition is unaffected by the removal of thermal conduction, which however significantly improves the agreement in terms of  $E_n$  at high velocity. Conversely, removing radiation closes the gap in terms of  $v_*$ , leaving the discrepancy of  $E_n$  at high velocity unchanged.

This is further supported by plotting the burn, thermal conduction and radiation loss contributions (in terms of power densities) for the Revolver design [2] using **FLAIM** (Figure 13). We can clearly see that radiation dominates over conduction during the implosion phase (before ignition), whilst conduction rapidly takes over in the burning regime (largely dominated by the electron component). We found the flux-limiting on thermal conduction (Equation 33) to have no impact on these results. This tells us that the simplified way in which the heat losses are treated is mainly responsible for the residual discrepancy we observe in the ignition maps. The burn operator in **FLAIM** shows virtually no difference with respect to the 1D description of the burn implemented in **B2**, suggesting very uniform conditions in the fuel capsule after ignition (a desirable feature for volume ignition, which is confirmed by inspecting the **B2** spatial profiles). This represents a significant advantage when dealing with simplified ignition models, because it removes the necessity of capturing the burn physics and the energy deposition in detail, for example, implementing methods for Charged Particle Transport (CPT) [47].

To conclude, this work also demonstrates that the potentially large discrepancy between a reduced simple model for volume ignition ICF and a multi-physics high-fidelity code can be removed almost entirely simply by treating the hydrodynamics correctly. As we have shown, heat losses do play an important role, but in the context of reduced models their accurate description is not strictly necessary since their impact can be roughly captured by simplified methods. Conversely, the same approach is less advisable when dealing with the hydrodynamic physics, which has a much stronger impact in determining the fuel conditions necessary for a robust ignition.

## 6. Modelling of the Revolver design

In this last section we use the **FLAIM** code to model the Revolver target [2, 3, 4], focusing on the last two layers of the structure, i.e. the pusher and the fuel. For a specific target, we assume the required pressure multiplication (originally supplied by the three-shell design) to be provided by FLF's proprietary amplifier technology. The initial conditions for Revolver in terms of geometry, implosion velocity (Table 2) and material states are reported in Section 4.1. The model choices are kept the same as those used in Section 5 (i.e., with all physics operators activated), except that we consider only the more accurate hydrodynamic model Hydro II (Table 1).

Figure 14 reports the temporal profiles of the main physical variables predicted by **FLAIM** for the two-layer Revolver design, with the B2 profiles also reported for reference. The results from **FLAIM** are compared to the work of Molvig et al. [3], which is based on 1D **HYDRA** [48] simulations of a laser-driven implosion of the *whole* Revolver target. Following Molvig et al. [2], the ignition criterion is based on the relative contribution of the fusion and the compressive power on the fuel internal energy  $u_f$ , due to the negligible radiative losses during the implosion. The earliest time in the simulation where the inequality<sup>9</sup>

$$\dot{Q}_{\text{fus}} \geq \frac{1}{4} \left( \dot{Q}_{\text{pdV}} + \frac{1}{V_f} \frac{dV_f}{dt} u_f \right) \quad (57)$$

holds defines the ignition time  $t_{\text{ign}}$ , where  $\dot{Q}_{\text{fus}}$  is given by Equation 45 and  $\dot{Q}_{\text{pdV}}$  by the sum over  $\{i, e, r\}$  and over the  $N_{c,f}$  fuel cells of Equation 21. The stagnation time  $t_{\text{stagn}}$  is the time at which the interface velocity  $v_1 = 0$ , before changing sign as the system expands. Finally, the peak burn time  $t_{\text{peak,b}}$  indicates the maximum of  $\dot{Q}_{\text{fus}}$ . **FLAIM** includes an integrated post-processor to extract relevant fiducial times, integrated quantities and general burn metrics. Table 4 presents the value of some diagnostic variables predicted by **FLAIM** at  $t_{\text{ign}}$ ,  $t_{\text{stagn}}$  and  $t_{\text{peak,b}}$ , compared with the ones reported in [3]. If not explicitly reported in the text of the reference work, the relevant quantities are extracted directly from the available plots and are to be considered approximate. Quantities for which it was not immediate to recover

---

<sup>9</sup>The additional term  $(1/V_f) (dV_f/dt) u_f$  in Equation 57 derives from the fact that the hydrodynamic operator evolves  $u_f$  and  $V_f$ , and both variations must be accounted for.

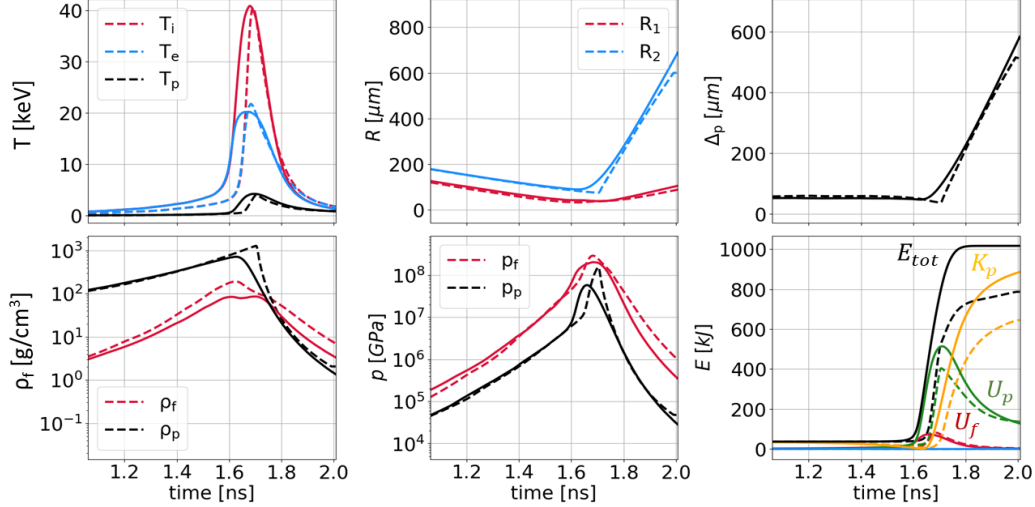


Figure 14: Temporal profiles of temperatures  $T_i, T_e, T_p$ , radii  $R_1, R_2$ , pusher thickness  $\Delta_p$  (top row). Fuel and pusher densities  $\rho_f, \rho_p$ , pressures  $p_f, p_p$ , and energy contributions (kinetic  $K_i$ , internal  $U_i$ , total  $E_{tot} = \sum_i U_i + K_i$ , for  $i \in \{f, p\}$ ) (bottom row). Solid line is FLAIM, dashed line is B2. Revolver design [3].

a reliable reference value at a specific time are not reported<sup>10</sup>.

From Table 4 we observe generally a good agreement between FLAIM and the reported number from the reference work. The ignition is a little delayed in FLAIM and occurs at a temperature slightly higher than the comparative value of  $\sim 2.5$  keV. At ignition, the pusher in FLAIM has  $\sim 60\%$  of the initial pusher kinetic energy, as opposed to  $\sim 80\%$  reported by Molvig et al. This suggests a stronger transfer of  $K_p$  to the fuel during the compression phase in FLAIM, and this is confirmed by the small overprediction in the fuel internal energy. Given the minimal impact of conductive losses during this phase (Figure 13), this probably indicates an underestimation of the radiation losses in FLAIM. This traps more heat inside the capsule and explains the higher ignition temperature and the slightly lower convergence ratio and fuel density (due to the higher adiabat).

It is worth noticing that the sum of the energies at ignition reported in [3]

<sup>10</sup>Following the work of Molvig et al. [3], ignition and deceleration onset are regarded as equivalent locations.

	Ignition			Stagnation			Peak burn		
	F	R	$\epsilon$	F	R	$\epsilon$	F	R	$\epsilon$
$t - t_0$ [ns]	0.4	0.35	0.14	0.57	0.5	0.14	0.64	0.54	0.18
$c_r$ [-]	5.9	6.5	0.09	7.9	9.3	0.15	/	/	/
$T_i$ [keV]	2.9	2.5	0.16	13.2	9.7	0.36	41	35	0.17
$T_e$ [keV]	2.9	2.5	0.16	13.2	9.7	0.36	20	20	0
$\rho_f$ [g/cm <sup>3</sup> ]	35	40	0.12	84	140	0.4	83	100	0.17
$\rho_p$ [g/cm <sup>3</sup> ]	427	400	0.07	693	2000	0.6	/	/	/
$U_f$ [kJ]	8	5	0.6	38	28	0.35	69	80	0.14
$U_p$ [kJ]	8	13	0.38	45	36	0.25	/	/	/
$K_p$ [kJ]	21	30	0.3	4	13	0.7	89	80	0.11

Table 4: Results for the Revolver design predicted by FLAIM (F) and reported in the reference work (R) of Molvig et al. [3].  $c_r = R_1^0/R_1$  is the convergence ratio. The relative error  $\epsilon = |y_F - y_R|/y_R$  is also reported.  $t_0$  is the time of shock convergence.

is more than the initial  $K_p \approx 37$  kJ characteristic of Revolver. This indicates some form of pre-heat during the implosion (e.g., radiation transport from the drive on the outer shells) that is not captured in FLAIM and explains the higher discrepancy observed for these quantities at ignition.

At stagnation all the quantities are correctly captured by FLAIM, except the pusher density which is a factor of  $\sim 3$  lower. However, the pusher density  $\rho_p \approx 2000$  g/cm<sup>3</sup> mentioned in the reference paper [3] is not entirely consistent to what reported in the corresponding plot at stagnation, in which a narrow peak at  $\rho_p \approx 2500$  g/cm<sup>3</sup> is visible, suggesting that a lower *average* density would be probably more accurate ( $\rho_p \approx 1000/1500$  g/cm<sup>3</sup>) and better in line with our results.

At peak burn the ion and electron temperatures separate and show very good agreement with Revolver, as well as the energy distribution between fuel and pusher. We measure a relative error of  $\sim 10 - 17\%$  for all variables at peak burn, which directly impact the prediction on the final burn metrics. Regarding this, FLAIM predicts a final neutron energy yield of  $E_n = 3.87$  MJ and a fuel burn fraction of  $\Phi_f = 0.57$ . Molvig et al. report a burn-up fraction

of  $\Phi_f^{\text{ref}} \approx 0.5$ , in reasonable agreement. Given that the maximum possible neutron energy yield from Revolver (assuming complete burn) is  $E_n^{\text{max}} = 6.75$  MJ, the value of  $\Phi_f^{\text{ref}}$  provides an estimated reference neutron energy yield  $E_n^{\text{ref}} = 3.4$  MJ, which is comparable with our result ( $\epsilon \approx 0.13$ ). This is consistent with the minor overestimation of  $E_n$  reported in Section 5 (Figure 9) and can be attributed to the simplified treatment of the heat losses in **FLAIM**, in particular thermal conduction, which dominates the heat losses in the burning regime (Section 5.1).

In conclusion, we find that **FLAIM** does indeed give suitably accurate results for such systems to be valuable as a predictive design tool, with the vast bulk of the physics captured by numerically inexpensive and simple models. This gives us confidence in our ability to use **FLAIM** as an accurate and robust surrogate for integrated simulations of volume ignition systems that we can leverage in large-scale optimisation and parameter space exploration.

## 7. Conclusions

In this work we have presented **FLAIM**, a reduced model for the compression and thermonuclear burn of a spherical DT fuel capsules with high-Z pushers, in the context of the volume ignition scheme. **FLAIM**'s modularity and extensibility lend it significant utility in the performance of rapid investigations and it is used extensively at FLF for global optimisation, sensitivity analyses and large parameter scans. **FLAIM** is computationally very fast (Appendix A), with typical simulations with all operators activated running in  $\sim 2 - 8$  s (with potential margin for improvement). This has allowed us to execute large optimisation campaigns comprised of tens of thousands of simulations, obtaining relevant results in just a few hours.

The objective of this work was to present **FLAIM** from the point of view of the physical and numerical modelling. **FLAIM** relaxes many of the assumptions commonly adopted in the reduced modelling of the volume ignition in ICF capsules, employing (i) hydrodynamic models independent of the type of EoS used as a closure; (ii) tabulated EoS and transport properties, accounting for the non-ideality typical of extreme physical conditions; (iii) a model for the wall able to track the radiation diffusion wave in the pusher based on the heat flux from the fuel; and (iv) a detailed thermonuclear burn operator which accounts for reactivity reduction, alpha-particle escape and pusher heating, as well as fuel depletion. Finally, we have implemented an additional hydrodynamic operator based on a 1D Lagrangian description of the fuel and pusher regions. This has been done to improve on the commonly used assumption of infinitesimally thin or constant-thickness pushers. The impact of this modification on the computational cost of a **FLAIM** simulation has been found to be very limited (Figure A.15d), given the inherent capability of Lagrangian descriptions of high convergence ratio implosions to provide very reliable results with low resolution. Moreover, the benefits in terms of physical accuracy outweigh the (minimal) cost. We compared pure hydrodynamic simulations using **FLAIM** to our in-house hydro code **B2** over a large parameter space, demonstrating that for relatively thick pushers an accurate description of the hydrodynamics is essential. A constant thickness pusher (or an infinitesimally thin one) greatly overestimates the compressive work done on the capsule, consuming all of its kinetic energy to increase the internal energy of the fuel. Whilst this assumption is reasonable for very thin pushers, it rapidly worsens the predictive capabilities of the model even for moderately thick ones. Conversely, a 1D description of the hydrodynamics



(even using a few cells) is able to correctly predict the compression work and the energy distribution between the fuel and the shell with a negligible increase in simulation run-time.

Another major advantage of considering a 1D description *only* for the hydrodynamics, is that all the other operators, that could be very complex to implement in a spatially-dependent framework, can be carried out as simple 0D models. An obvious example is the burn operator, for which a full 1D description would also require equations to govern the transport of species ( $\alpha$  particles in particular) across the whole domain. In FLAIM this is not necessary and simple models available in literature can be used to estimate the fraction of particles that leave the fuel region based on the capsule size. Contrary to what we observed for the hydrodynamics, the impact of this approach for the burn physics is actually very limited and entirely justifiable. To support this, we ran a simulation scan (including hydrodynamics, burn and losses) comparing the results obtained from FLAIM and B2, showing good agreement in terms of final neutron yield and burn fraction in the whole parameter space. We found that the residual discrepancies are attributable to the way the heat losses are treated in the model. Specifically, we found the approximate model for thermal conduction to govern the FLAIM-B2 discrepancy in the main ignition region, where we know the conductive fluxes dominate over radiation. Conversely, our simplified radiation model mainly impacts the boundaries of the ignition region, but not the accuracy in terms of burn performance metrics (i.e., neutron yield and burn fraction).

Finally, we used FLAIM to model the Revolver design, showing good agreement with literature results for some selected key variables evaluated at ignition, stagnation and peak burn. For the latter, we report errors of  $\sim 10-17\%$  for all the quantities investigated, increasing our assurance in the reliability of FLAIM as an accurate surrogate for predicting target performance in the peak burn phase.

Future work will focus on closing the existing gap between FLAIM and 1D high-fidelity simulations, mainly focusing on the heat loss models. Further optimisations include the implementation of alternative solutions for the integration of the ODE system, as well as improvements regarding the computational cost and residual code overhead.

## Appendix A. Spatial convergence

The Revolver design [2] presented in Section 6 is run with FLAIM at different spatial resolutions to evaluate the convergence behaviour. The error is evaluated based on the values of the final neutron yield  $Y_n$  and the maximum ion temperature  $T_i$ . The value at zero grid spacing is estimated by the Richardson extrapolation [49] of the quantities of interest. Using a *constant* refinement ratio  $r$  ( $r = 2$  in our case), the observed order of convergence  $p$  is

$$p_y = \frac{\ln\left(\frac{y_3 - y_2}{y_2 - y_1}\right)}{\ln(r)} \quad \text{for } y \in \{Y_n, T_i\}, \quad (\text{A.1})$$

where  $y_1, y_2, y_3$  are values of the metric  $y$  at three *decreasing* grid resolutions. If  $p > 0$  (i.e., the solution is converging), the Richardson extrapolation value  $y_0$  can be computed as

$$y_0 \cong y_{\text{Rich}} = y_1 + \frac{y_1 - y_2}{r^p - 1}, \quad (\text{A.2})$$

and the estimated relative error for a number of simulations  $N_{\text{sims}} \geq 3$  is computed as

$$\epsilon_i = \frac{|y_i - y_0|}{y_0} \quad \text{for } i = 0, \dots, N_{\text{sims}}. \quad (\text{A.3})$$

Figure A.15 reports the plot of  $\epsilon_i$  vs. the number of cells<sup>11</sup> in the fuel (a), in the pusher (b) and total (c).

All simulation metrics show good convergence properties, with orders  $0.9 \lesssim p \lesssim 2$ . The observed order of convergence is affected by the time stepping scheme, currently first order, as well as by the presence of hydrodynamic discontinuities, i.e. shocks. Interestingly, the convergence order is different when refining the fuel and the pusher region independently, whereas an intermediate order is observed when both are changed at the same time.

The elapsed time (Figure A.15d) remains below 30 s for the most resolved case. Using  $N_c = 80$ , we can obtain well-resolved (and converged) simulations ( $\epsilon_i \approx 0.01$ ) at a cost ( $t_{\text{elapsed}} \approx 8$  s) comparable to what provided by the non-discretised model Hydro I ( $t_{\text{elapsed}} \approx 6$  s). To give a reference, an equivalent

---

<sup>11</sup>The size of the grid cells is not relevant for this analysis, since it is not constant for moving grids.

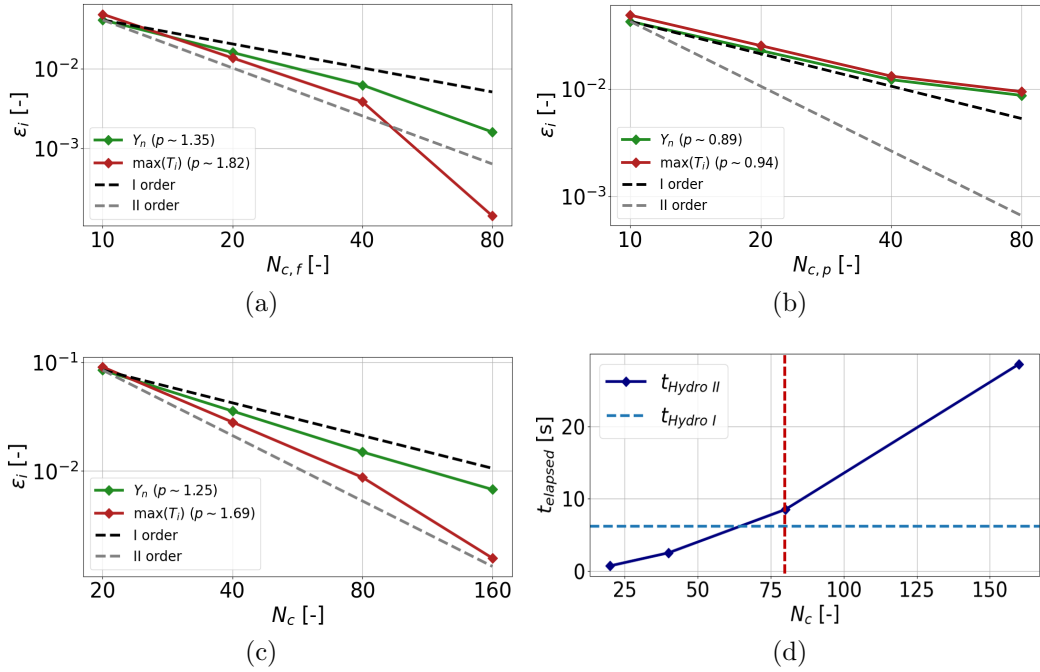


Figure A.15: Grid convergence analysis on the number of cells in the fuel (a) (with  $N_{c,p} = 80$ ), on the number of cells in the pusher (b) (with  $N_{c,f} = 80$ ), on the total number of cells  $N_c$  (c). The observed orders of convergence are reported in the legend for  $Y_n$  and  $\max(T_i)$ . Total elapsed time is shown in (d) for the simulations shown in (c) run with models Hydro I, II. The vertical dashed red line in (c) indicates the resolution  $N_c = 80$  typically used for FLAIM simulations.

converged 1D B2 simulation of the Revolver design showed  $t_{\text{elapsed}} \approx 3$  h. For the scan in Table 2, all 125 simulations were launched in parallel for the two codes, with an elapsed time of  $\sim 5$  h for B2 and  $\sim 10$  s for FLAIM (both governed by the slowest simulation), highlighting the advantages of using FLAIM for quickly run large parameter scans and sensitivity analyses that often require thousands of simulations.

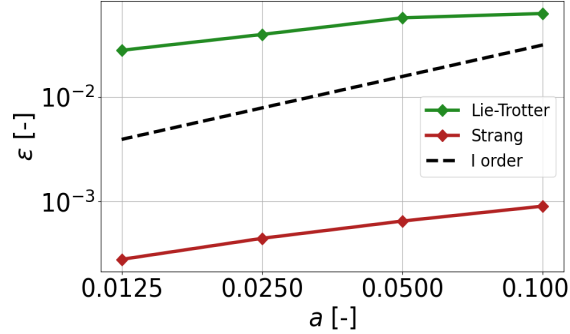


Figure B.16: Convergence analysis for the average distance  $\epsilon$  between the  $T_i(t)$  profiles generated by different physical operator ordering (Equation B.1).

## Appendix B. Operator ordering

When adopting an operator splitting approach for the solution of an ODE system, one carries numerical errors due to the decoupling on the physical operators. Moreover, it is inevitable to obtain different solutions for different choices of the operator ordering. However, one must ensure that this discrepancy vanishes for increasing resolution of the time discretisation, effectively leading to a code that produces consistent results independent of the specific order of the physical operators involved. To this purpose, we ran a simple test:

- The Revolver design (Section 6) is run  $N_{\text{sims}}$  times, with different randomly generated operator ordering ( $N_{\text{sims}} = 4$ ). The physical operators are 6, i.e. hydrodynamics, thermal-equilibration, conduction, radiation, wall, burn (Section 2);
- For these  $N_{\text{sims}}$  simulations, the error  $\epsilon$  (interpreted as the average distance between them) is calculated by means of the average of the  $L_2$  norms of the ion temperature profiles  $T_i(t)$  (taking one of them as the

reference) using

$$\begin{aligned}
\epsilon &= \\
&= \frac{1}{N_{\text{sims}}} \sum_j^{N_{\text{sims}}} L_2(T_{i,j}) \\
&= \frac{1}{N_{\text{sims}}} \sum_j^{N_{\text{sims}}} \sqrt{\sum_k^{N_{\text{steps},j}} \left( \frac{T_{\text{ref}}(t_k) - T_{i,j}(t_k)}{T_{\text{ref}}(t_k)} \right)^2} \quad ;
\end{aligned} \tag{B.1}$$

- The procedure is applied at decreasing Courant numbers  $a$  (Equation 51) to verify the convergence properties of  $\epsilon$ .

The analysis is done for both the Lie-Trotter and the Strang splitting presented in Section 3 and Figure B.16 summarises the results. The average value  $\epsilon$  is in general very low ( $10^{-1} \gtrsim \epsilon \gtrsim 10^{-4}$ ) and, as expected, shows the lowest values for the Strang splitting. The different profiles  $T_i(t)$  converge with time resolution, allowing us to conclude that FLAIM results are effectively independent of the operator ordering.

## Appendix C. The B2 code

In this paper the B2 code is extensively used as a benchmark code for assessing the reliability of FLAIM as a reduced volume ignition model. B2 is one of FLF’s main production codes for the design of our targets and it is continuously and extensively verified against a suite of benchmark test-cases and validated with in-house and external experimental results. We present here a brief description of the main physical models implemented in B2, as well as some selected verification tests relevant to support this work.

B2 is an Eulerian 3D parallel multi-material RMHD (Resistive-Magneto-Hydrodynamic) code adopting structured orthogonal grids. The hydrodynamics is based on a Lagrangian remap approach with artificial viscosity, coupled with a geometric Volume Of Fluid (VOF) methodology for the interface capturing [50] (using a Simple Line Interface Calculation (SLIC) method for the local interface reconstruction). Several radiation transport models are available (multi-group radiation transport, with  $\mathbb{P}_{1/3}$  or radiation diffusion closure and an exact 6D Monte Carlo transport), whilst thermal conduction is applied to both ion and electron species, accounting for flux-limiting. The thermonuclear burn model includes fuel depletion and single-group Eulerian  $\alpha$  particle diffusion to describe the fusion self-heating [47]. EoS and transport properties are tabulated for temperatures up to  $T_i = 100$  keV and, since they are shared between B2 and FLAIM, the details about their calculation have been already reported in Section 2.

### *Appendix C.1. Hydrodynamics*

Lagrangian remap [51] is adopted to model the hydrodynamics, solving the generalised two-temperature Euler equations for mass, momentum and total energy conservation. The hydrodynamic scheme is based on a first-order Godunov formulation (which is the one used in this work), but higher-order reconstruction schemes (up to third-order) are also available. We report two classic verification tests for hydrodynamics: (i) Sod shocks [52] and (ii) Noh implosions [53].

#### *Appendix C.1.1. Sod shocks*

This is a standard test for hydrodynamic solvers, consisting of a 1D Riemann problem that, when evolved in time, produces five distinct regions with a shock, a rarefaction and a contact discontinuity. The five test cases presented in this Appendix are extensively described in Toro et al. [54] (using an adiabatic index  $\gamma = 5/3$ ), and the results are reported in Figure C.17.

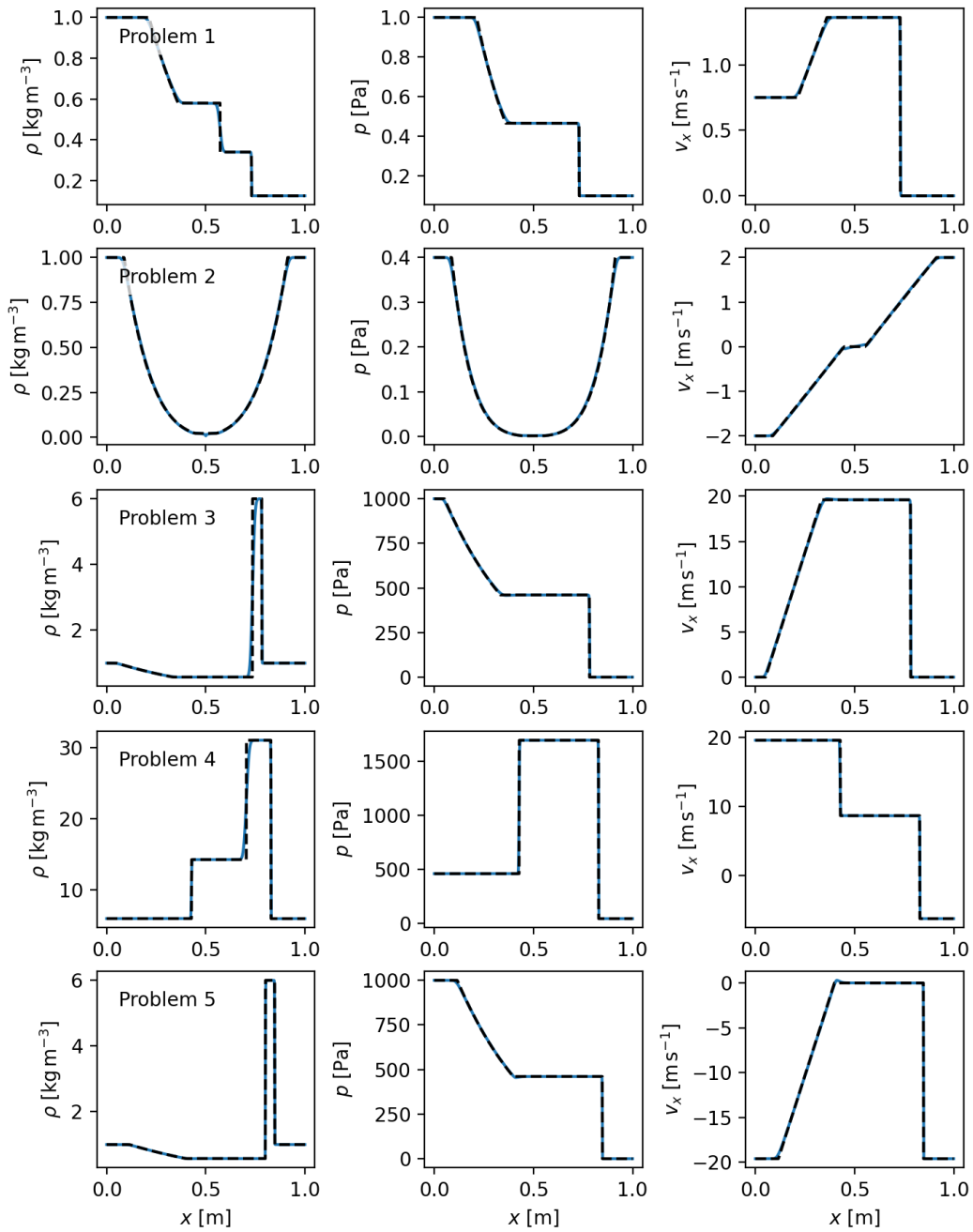


Figure C.17: Sod shocks: comparison between B2 (blue solid line) and the analytic solution (black dashed line) in terms of spatial profiles of mass density  $\rho$ , pressure  $p$  and fluid velocity  $v_x$  for the 5 problems reported in Toro et al. [54]. For all cases,  $n_c = 2048$  and 1<sup>st</sup> order Godunov scheme is used.



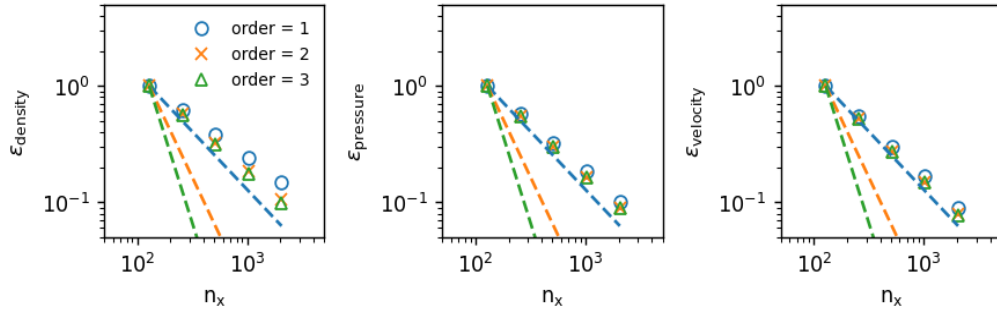


Figure C.18: Sod shocks: grid convergence properties of B2 for Sod problem 1 (Figure C.17, top row), using three different hydrodynamic schemes with 1<sup>st</sup>, 2<sup>nd</sup> and 3<sup>rd</sup> theoretical order of accuracy.

Convergence properties of the B2 code for the Sod 1 problem are shown in Figure C.18 using three hydrodynamic schemes at different orders of convergence (using a standard normalised  $L_1$  norm to measure the error  $\epsilon$ ). The discontinuous nature of the solution and the first-order time stepping scheme limit the observed convergence to be  $\sim 1^{\text{st}}$  order, as expected.

#### Appendix C.1.2. Noh implosions

The Noh implosion test case [53] exercises hydrodynamics, convergent geometry and implosion physics in planar, axial or spherical geometry. In a domain  $0 \leq x \leq 1$ , a cold ideal gas ( $\gamma = 5/3$ ) at initially zero pressure and temperature falls inwards at constant velocity ( $v = -1$  m/s) and stagnates on the axis, producing an expanding shock front propagating into the collapsing gas. It is known to be a very challenging test for ICF codes, with most codes reporting errors in the form of wall heating, lack of symmetry, incorrect shock speeds or even failure to run [55]. Results are shown in Figures C.19, C.20, C.21 for a planar, axial and spherical geometry respectively. The plots show good agreement with the analytic results, except for the region near the axis, where classic wall overheating can be noticed [56]. As for the Sod shock test cases, the convergence analysis is carried out in terms of standard normalised  $L_1$  norm and it is reported in Figure C.22, showing  $\sim 1^{\text{st}}$  order convergence.

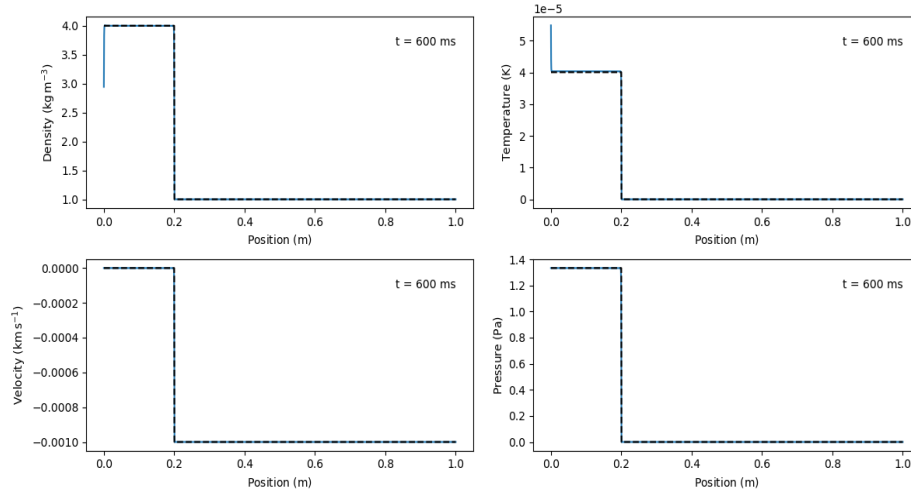


Figure C.19: Noh implosion (planar) [53]: mass density, temperature, velocity and pressure spatial profiles, comparison between B2 (blue solid line,  $n_c = 2048$ ) and the analytic solution (black dashed line).

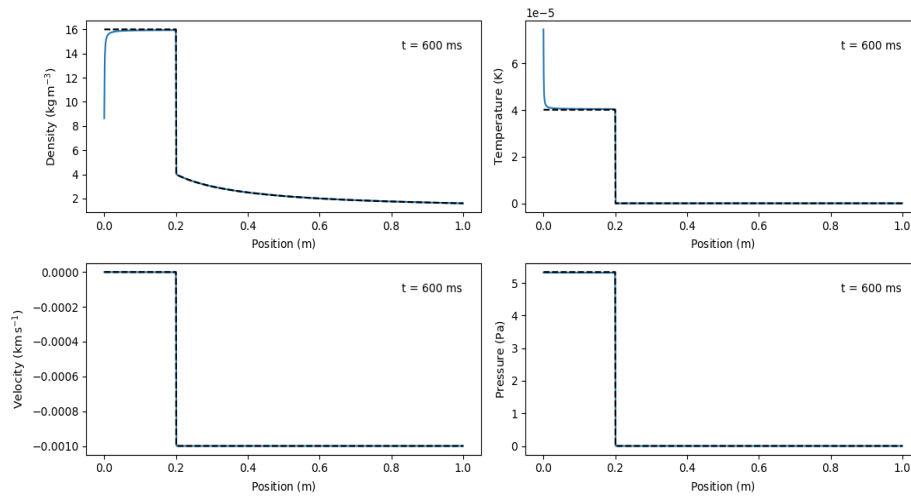


Figure C.20: Noh implosion (axial) [53]: mass density, temperature, velocity and pressure spatial profiles, comparison between B2 (blue solid line,  $n_c = 2048$ ) and the analytic solution (black dashed line).

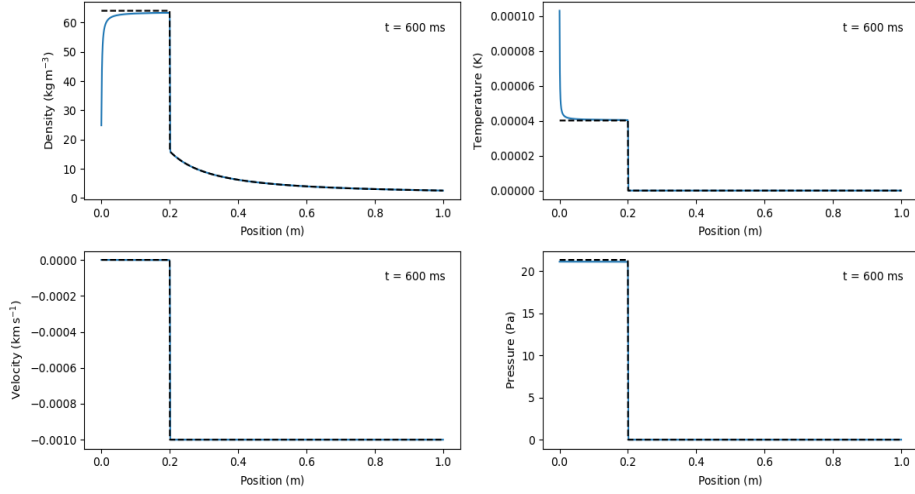


Figure C.21: Noh implosion (spherical) [53]: mass density, temperature, velocity and pressure spatial profiles, comparison between B2 (blue solid line,  $n_c = 2048$ ) and the analytic solution (black dashed line).

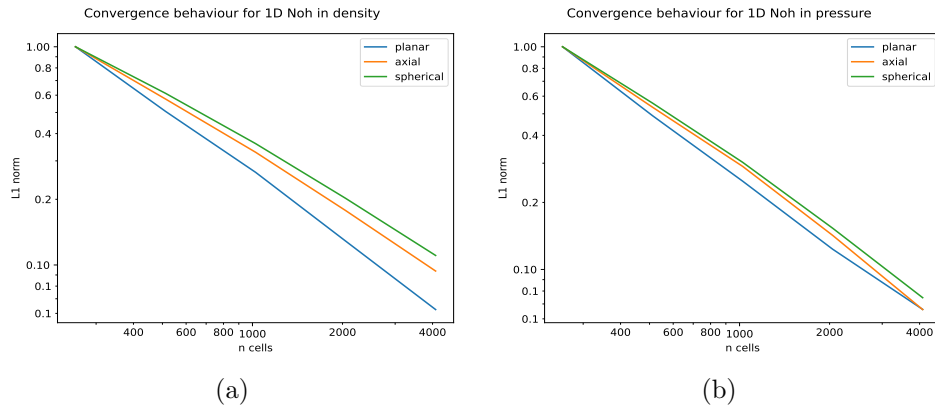


Figure C.22: Noh implosions: convergence properties of B2 for planar, axial and spherical geometry.

### *Appendix C.2. Thermal conduction*

A standard flux-based finite-volume formulation for ion and electron thermal conduction is implemented in B2, augmented with flux-limiters to account for the upper limit on the heat flux given by the particle thermal speed. The benchmark test cases we present here are (i) a simple thermal relaxation test and (ii) the Zel’dovich and Raizer thermal wave verification test [57].

#### *Appendix C.2.1. Thermal relaxation*

This test models the relaxation of a small Gaussian temperature perturbation. For a single temperature system with constant thermal conductivity, a closed-form solution can be derived. A 1D domain [ $-10 \text{ mm} \leq x \leq 10 \text{ mm}$ ], with a constant background density, has a temperature profile initialised as

$$T(x) = T_0 + T_1 e^{-\left(\frac{x}{w}\right)^2}, \quad (\text{C.1})$$

with  $T_0 = 100 \text{ eV}$ ,  $T_1 = 10 \text{ eV}$  and  $w = 1 \text{ mm}$ . The thermal conductivity is set to  $\kappa_0 = 57000 \text{ W/m/K}$  (this approximates the Spitzer electron thermal conductivity of a fully ionised helium plasma at  $T = T_0$ ), whilst the volumetric heat capacity is fixed to  $c_v = 520 \text{ J/m}^3/\text{K}$ . The analytic solution for the 1D transient heat diffusion equation is

$$T(x, t) = T_0 + T_1 \left(\frac{w}{w_0}\right) e^{-\left(\frac{x}{w_0}\right)^2}, \quad (\text{C.2})$$

where  $w_0 = \sqrt{w^2 + 4\kappa_0 t/c_v}$ . The comparison between the B2 simulation and the analytic solution is reported in Figure C.23a.

#### *Appendix C.2.2. Zel’dovich-Raizer thermal wave*

This test is based on a self-similar solution to thermal wave propagation in a cold medium with a non-linear thermal conductivity, as described in Chapter 10 of Zel’dovich and Raizer’s textbook [57]. The domain spans  $0 \leq x \leq 100 \mu\text{m}$ , the EoS is deuterium ideal gas ( $\gamma = 5/3$ ) and the thermal conductivity depends on temperature following  $\kappa = \zeta c_v T^n$  (with  $c_v$  being the volumetric heat capacity,  $\zeta = 1 \text{ m}^2/\text{s}/\text{K}^n$  and  $n = 5/2$ ). The analytic solution is given by Eqs. (10.32)-(10.33) in [57]. The wave dynamics is reported in Figure C.23b in terms of spatial temperature profiles at different time instants.

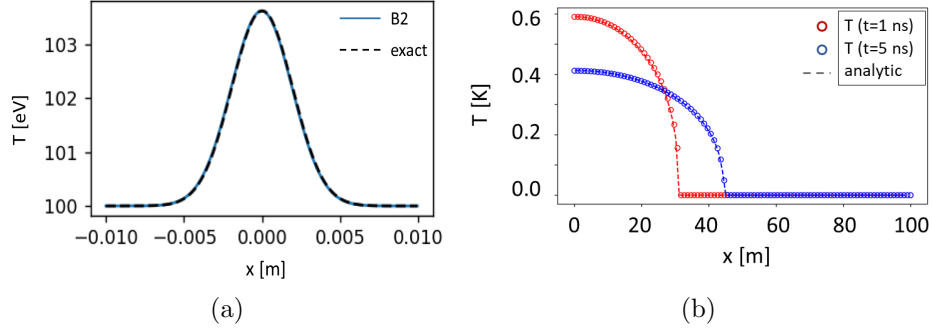


Figure C.23: Thermal conduction verification tests: thermal relaxation (a) at  $t = 15$  ns and Zel'dovich-Raizer thermal wave (b), both showing the spatial profiles of temperature obtained with B2 vs. the corresponding analytic solution.

### Appendix C.3. Radiation diffusion

As reported in the introduction of this section, several models are available in B2 for modelling radiation transport. In this work, the standard radiation diffusion approach [58] has been used for the comparisons in Section 5 in order to be consistent with the wall model [9, 29] implemented in FLAIM (which provides a semi-analytic solution for a 1D radiation diffusion equation in the shell). The McClarren solution is adopted for verification purposes [59].

#### Appendix C.3.1. McClarren test case

McClarren [59] provides an analytic solution for a two-group Marshak wave with spatially constant opacities  $\chi_1, \chi_2$ . Given a symmetric 1D domain, a line-source of radiation is applied to a fixed region  $-z_0/2 \leq z \leq z_0/2$  around the origin for a short time ( $\tau < \tau_0$ , with  $\tau = c\chi_1 t$ ), after which it is switched off, letting the radiation diffuse towards the boundaries. The test verifies that (i) two radiation groups can be transported correctly under the diffusion approximation and that (ii) the radiative energy density of the groups is correctly coupled with the internal energy density of the medium via absorption and emission. The results are reported in Figure C.24.

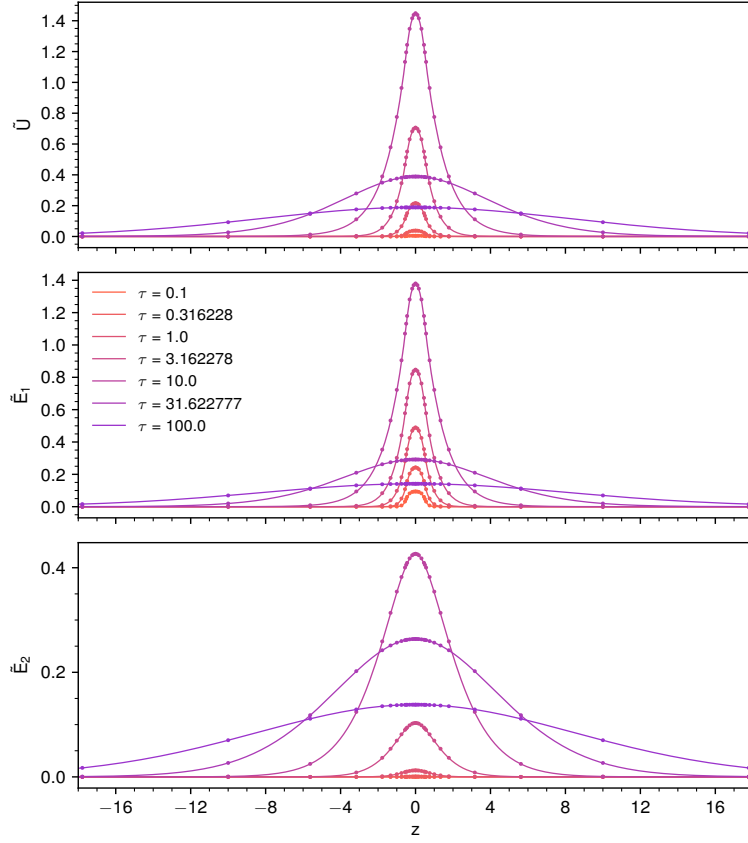


Figure C.24: McClarren test case [59]:  $\tilde{E}_i = E_i / (aT_H^4)$  is the normalised radiative energy densities for group  $i$ , whilst  $\tilde{U} = U / (aT_H^4)$  is the normalised internal energy density of the medium. The holraum temperature is  $T_H = 1$  keV. Analytic solution (dots) vs. B2 simulation (solid line).

## References

- [1] First Light Fusion Ltd., <https://firstlightfusion.com/>, accessed: March 1, 2024 (2024).
- [2] K. Molvig, M. J. Schmitt, B. J. Albright, E. S. Dodd, N. M. Hoffman, G. H. McCall, S. D. Ramsey, Low fuel convergence path to direct-drive fusion ignition, *Physical Review Letters* 116 (2016) 255003. doi:10.1103/PhysRevLett.116.255003.
- [3] K. Molvig, M. J. Schmitt, R. Betti, E. M. Campbell, P. McKenty, Stable and confined burn in a Revolver ignition capsule, *Physics of Plasmas* 25 (2018) 082708. doi:10.1063/1.5037224.  
URL <https://doi.org/10.1063/1.5037224>
- [4] B. D. Keenan, W. T. Taitano, K. Molvig, Physics of the implosion up until the time of ignition in a revolver (triple-shell) capsule, *Physics of Plasmas* 27 (2020) 042704.
- [5] K. Lackner, S. Colgate, N. Johnson, R. Kirkpatrick, R. Menikoff, A. Petschek, Equilibrium ignition for icf capsules, in: *AIP Conference Proceedings*, Vol. 318, American Institute of Physics, 1994, pp. 356–361.
- [6] R. C. Kirkpatrick, An overview of design space for small fusion targets, *Nuclear Fusion* 19 (1979) 69.
- [7] R. C. Kirkpatrick, J. A. Wheeler, The physics of DT ignition in small targets, *Nuclear Fusion* 21 (1981) 389.
- [8] C.-K. Huang, K. Molvig, B. J. Albright, E. S. Dodd, E. L. Vold, G. Kagan, N. M. Hoffman, Study of the ion kinetic effects in ICF runaway burn using a quasi-1D hybrid model, *Physics of Plasmas* 24 (2017) 022704.
- [9] E. S. Dodd, K. Molvig, C. Chung, B. J. Albright, A model for radiative heating of a high-Z pusher, *Physics of Plasmas* 27 (2020) 072702.
- [10] S. Atzeni, 2-d lagrangian studies of symmetry and stability of laser fusion targets, *Computer Physics Communications* 43 (1) (1986) 107–124.
- [11] S. Faik, A. Tauschwitz, I. Iosilevskiy, The equation of state package FEOS for high energy density matter, *Computer Physics Communications* 227 (2018) 117.

- [12] R. M. More, K. H. Warren, D. A. Young, G. B. Zimmerman, A new quotidian equation of state (QEOS) for hot dense matter, *Physics of Fluids* 31 (1988) 3059.
- [13] R. Betti, M. Umansky, V. Lobatchev, V. Goncharov, R. McCrory, Hot-spot dynamics and deceleration-phase rayleigh–taylor instability of imploding inertial confinement fusion capsules, *Physics of Plasmas* 8 (12) (2001) 5257–5267.
- [14] R. Betti, K. Anderson, V. Goncharov, R. McCrory, D. Meyerhofer, S. Skupsky, R. Town, Deceleration phase of inertial confinement fusion implosions, *Physics of Plasmas* 9 (5) (2002) 2277–2286.
- [15] R. C. Kirkpatrick, C. C. Cremer, L. C. Madsen, H. H. Rodgers, R. S. Cooper, Structured fusion target designs, *Nuclear Fusion* 15 (1975) 333.
- [16] J. VonNeumann, R. D. Richtmyer, A method for the numerical calculation of hydrodynamic shocks, *Journal of applied physics* 21 (3) (1950) 232–237.
- [17] A. E. Mattsson, W. J. Rider, Artificial viscosity: back to the basics, *International Journal for Numerical Methods in Fluids* 77 (7) (2015) 400–417.
- [18] G. Hazak, Z. Zinamon, Y. Rosenfeld, M. W. C. Dharma-wardana, Temperature relaxation in two-temperature states of dense electron-ion systems, *Physical Review E* 64 (2001) 066411.
- [19] D. O. Gericke, Kinetic approach to temperature relaxation in dense plasmas, *Journal of Physics: Conference Series* 11 (2005) 111.
- [20] M. S. Murillo, M. W. C. Dharma-wardana, Temperature relaxation in hot dense hydrogen, *Physical Review Letters* 100 (2008) 205005.
- [21] J. Vorberger, D. O. Gericke, Comparison of electron-ion energy transfer in dense plasmas obtained from numerical simulations and quantum kinetic theory, *High Energy Density Physics* 10 (2014) 1.
- [22] D. O. Gericke, M. S. Murillo, M. Schlanges, Dense plasma temperature equilibrium in the binary collision approximation, *Physical Review E* 65 (2002) 036418.



- [23] J. Daligault, G. Dimonte, Correlation effects on the temperature-relaxation in dense plasmas, *Physical Review E* 79 (2009) 056403.
- [24] J. Daligault, D. Mozyrsky, Ion dynamics and energy relaxation in nonequilibrium electron-ion systems, *Physical Review E* 75 (2007) 026402.
- [25] D. A. Chapman, J. Vorberger, D. O. Gericke, Reduced coupled-mode approach to electron-ion energy relaxation, *Physical Review E* 88 (2013) 013102.
- [26] M. W. C. Dharma-wardana, F. Perrot, Energy relaxation and the quasiequation of state of a dense two-temperature nonequilibrium plasma, *Physical Review E* 3705 (1998) 58.
- [27] J. Vorberger, D. O. Gericke, Coupled mode effects on energy transfer in weakly coupled, two-temperature plasmas, *Physics of Plasmas* 16 (2009) 082702.
- [28] J. Vorberger, D. O. Gericke, T. Bornath, M. Schlanges, Energy relaxation in dense, strongly coupled two-temperature plasma, *Physical Review E* 81 (2010) 046404.
- [29] J. H. Hammer, M. D. Rosen, A consistent approach to solving the radiation diffusion equation, *Physics of Plasmas* 10 (2003) 1829. doi:<https://doi.org/10.1063/1.1564599>.
- [30] A. R. Fraser, Crilly, N.-P. A. J., Niasse, J. D. Pecover, D. A. Chapman, S. J. O'Neill, J. Chittenden, SpK: A fast atomic physics code for generating global equation of state and opacity models for use in high-energy-density physics simulations, *High Energy Density Physics* (Submitted 2024).
- [31] R. Malone, R. McCrory, R. Morse, Indications of strongly flux-limited electron thermal conduction in laser-target experiments, *Physical Review Letters* 34 (12) (1975) 721.
- [32] N. T. Mitchell, D. A. Chapman, C. J. McDevitt, M. P. Read, G. Kagan, A reduced kinetic method for investigating non-local ion heat transport in ideal multi-species plasmas, *Plasma Physics and Controlled Fusion* (Submitted 2024).

- [33] L. G. Stanton, M. S. Murillo, Ionic transport in high-energy-density matter, *Physical Review E* 93 (2016) 043203.
- [34] Y. T. Lee, R. M. More, An electron conductivity model for dense plasmas, *Physics of Fluids* 27 (1984) 1273.
- [35] N. M. Hoffman, G. B. Zimmerman, K. Molvig, H. G. Rinderknecht, M. J. Rosenberg, B. J. Albright, A. N. Simakov, H. Sio, A. B. Zylstra, M. G. Johnson, F. H. Séguin, J. A. Frenje, C. K. L. R. D. Petrasso, D. M. Higdon, G. Srinivasan, V. Y. Glebov, C. Stoeckl, W. Seka, T. C. Sangster, Approximate model for the ion-kinetic regime in inertial-confinement-fusion capsule implosions, *Physics of Plasmas* 22 (2015) 052707. doi:<https://doi.org/10.1063/1.4921130>.  
URL <https://aip.scitation.org/doi/10.1063/1.4921130>
- [36] G. Fraley, E. Linnebur, R. Mason, R. Morse, Thermonuclear burn characteristics of compressed deuterium-tritium microspheres, *The Physics of Fluids* 17 (2) (1974) 474–489.
- [37] P. Woodward, Compton interaction of a photon gas with a plasma, *Physical Review D* 1 (10) (1970) 2731.
- [38] K. Molvig, M. Alme, R. Webster, C. Galloway, Photon coupling theory for plasmas with strong Compton scattering: Four temperature theory, *Physics of Plasmas* 16 (2009) 023301.
- [39] O. N. Krokhin, V. B. Rozanov, Escape of  $\alpha$  particles from a laser-pulse-initiated thermonuclear reaction, *Soviet Journal of Quantum Electronics* 2 (4) (1973) 393.
- [40] H.-S. Bosch and G. M. Hale, Improved formulas for fusion cross-sections and thermal reactivities, *Nuclear Fusion* 32 (4) (1992) 611.
- [41] K. Molvig, N. M. Hoffman, B. J. Albright, E. M. Nelson, R. B. Webster, Knudsen Layer Reduction of Fusion Reactivity, *Physical Review Letters* 109 (2012) 095001.
- [42] B. J. Albright, K. Molvig, C.-K. Huang, A. N. Simakov, E. S. Dodd, N. M. Hoffman, G. Kagan, P. F. Schmit, Revised Knudsen-layer reduction of fusion reactivity, *Physics of Plasmas* 20 (2013) 122705.

- [43] G. S. Fraley, E. J. Linnebur, R. J. Mason, R. L. Morse, Thermonuclear burn characteristics of compressed deuterium-tritium microspheres, *Physics of Fluids* 17 (1974) 474. doi:10.1063/1.1694739.
- [44] S. Atzeni, J. Meyer-ter-Vehn, *The Physics of Inertial Fusion*, Oxford University Press, 2004.
- [45] H. F. Trotter, On the product of semi-groups of operators, *Proceedings of the American Mathematical Society* 10 (4) (1959) 545–551.
- [46] G. Strang, On the construction and comparison of difference schemes, *SIAM journal on numerical analysis* 5 (3) (1968) 506–517.
- [47] S. Atzeni, A. Caruso, A diffusive model for alpha-particle energy transport in a laser plasma, *Nuovo Cimento B Serie* 64 (1981) 383–395.
- [48] M. M. Marinak, G. Kerbel, N. Gentile, O. Jones, D. Munro, S. Pollaine, T. Dittrich, S. Haan, Three-dimensional hydra simulations of national ignition facility targets, *Physics of Plasmas* 8 (5) (2001) 2275–2280.
- [49] P. J. Roache, P. M. Knupp, Completed richardson extrapolation, *Communications in Numerical Methods in Engineering* 9 (5) (1993) 365–374.
- [50] C. W. Hirt, B. D. Nichols, Volume of fluid (vof) method for the dynamics of free boundaries, *Journal of computational physics* 39 (1) (1981) 201–225.
- [51] T. Arber, A. Longbottom, C. Gerrard, A. Milne, A staggered grid, lagrangian–eulerian remap code for 3-d mhd simulations, *Journal of Computational Physics* 171 (1) (2001) 151–181.
- [52] G. A. Sod, A survey of several finite difference methods for systems of nonlinear hyperbolic conservation laws, *Journal of computational physics* 27 (1) (1978) 1–31.
- [53] W. F. Noh, Errors for calculations of strong shocks using an artificial viscosity and an artificial heat flux, *Journal of Computational Physics* 72 (1) (1987) 78–120.
- [54] E. F. Toro, *Riemann solvers and numerical methods for fluid dynamics: a practical introduction*, Springer Science & Business Media, 2013.

- [55] R. Ramani, S. Shkoller, A fast dynamic smooth adaptive meshing scheme with applications to compressible flow, *Journal of Computational Physics* 490 (2023) 112280.
- [56] W. J. Rider, Revisiting wall heating, *Journal of Computational Physics* 162 (2) (2000) 395–410.
- [57] Y. B. Zeldovich, Y. P. Raizer, *Physics of Shock Waves and High Temperature Hydrodynamic Phenomena*, Dover, Mineola, NY, 2002.
- [58] G. C. Pomraning, *The Equations of Radiation Hydrodynamics*, Courier Corporation, 2005.
- [59] R. G. McClarren, Two-group radiative transfer benchmarks for the non-equilibrium diffusion model, *Journal of Computational and Theoretical Transport* 50 (6-7) (2021) 583–597.